HHS Public Access

Author manuscript

Cell. Author manuscript; available in PMC 2024 March 30.

Published in final edited form as:

Cell. 2023 March 30; 186(7): 1448–1464.e20. doi:10.1016/j.cell.2023.02.032.

A neutrophil response linked to tumor control in immunotherapy

Jeremy Gungabeesoon[1,12], **Nicolas A. Gort-Freitas**[2,12], **Máté Kiss**[3,4,12], **Evangelia Bolli**[2,3,4], **Marius Messemaker**[1,5], **Marie Siwicki**[1], **Mehdi Hicham**[3,4], **Ruben Bill**[2,3,4], **Peter Koch**[1], **Chiara Cianciaruso**[2,3,4], **Florent Duval**[3,4], **Christina Pfirschke**[1], **Michael Mazzola**[6], **Solange Peters**[7,8], **Krisztian Homicsko**[4,9,10,11], **Christopher Garris**[1], **Ralph Weissleder**[1,2], **Allon M. Klein**[2,13,*], **Mikael J. Pittet**[1,3,4,9,11,13,14,*]

[1]Center for Systems Biology, Massachusetts General Hospital Research Institute and Harvard Medical School, Boston, USA

[2]Department of Systems Biology, Harvard Medical School, Boston, USA

[3]Department of Pathology and Immunology, University of Geneva, Geneva, Switzerland

[4]AGORA Cancer Research Center, Lausanne, Switzerland

[5]Division of Molecular Oncology and Immunology, Netherlands Cancer Institute, Amsterdam, Netherlands

[6]Center for Regenerative Medicine, Massachusetts General Hospital, Boston, USA

[7]Service of Medical Oncology, Department of Oncology, CHUV, Lausanne, Switzerland

[8]Department of Oncology, University of Lausanne, Lausanne, Switzerland

[9]Ludwig Institute for Cancer Research, Lausanne, Switzerland

[10]Department of Oncology, CHUV, Lausanne, Switzerland

[11]Swiss Cancer Center Leman, Lausanne, Switzerland

[12]These authors contributed equally to this work

[13]Senior author

[14]Lead contact

[*]Correspondence: mikael.pittet@unige.ch and Allon_Klein@hms.harvard.edu.

Author Contributions

J.G. and M.J.P. initiated the study. J.G., M.J.P. and M.K. designed experiments. M.K. wrote the original draft. M.J.P., A.M.K., J.G., N.A.G.-F. and M.K. prepared the figures and wrote the manuscript. J.G., M.K., M.S., R.B., P.K., C.C., E.B., C.P., M.Ma., M.H., F.D. performed mouse experiments and related analyses. N.A.G.-F. carried out genomic data analysis. M.Me designed the TotalSeq experiment and provided code for data analysis. K.H. and S.P. provided human data. R.W. and C.G. provided input for research design and interpretation. M.J.P. and A.M.K designed analytical strategies, and supervised experiments and data analysis.

Declaration of Interests

M.J.P. has served as consultant for AstraZeneca, Elstar Therapeutics, ImmuneOncia, KSQ Therapeutics, Merck, Siamab Therapeutics, Third Rock Ventures., and Tidal. R.W. has served as a consultant for Moderna, Lumicell, Seer Biosciences, Earli, and Accure Health. The wife of R.B. is an employee and shareholder of CSL Behring and R.B. received a speaker's fee from Janssen.

Summary

Neutrophils accumulate in solid tumors and their abundance correlates with poor prognosis. Neutrophils are not homogenous, however, and could play different roles in cancer therapy. Here, we investigated the role of neutrophils in immunotherapy leading to tumor control. We show that successful therapies acutely expanded tumor neutrophil numbers. This expansion could be attributed to a *Sell*^{hi} state, rather than to other neutrophils that accelerate tumor progression. Therapy-elicited neutrophils acquired an interferon gene signature, also seen in human patients, and appeared essential for successful therapy, as loss of the interferon-responsive transcription factor IRF1 in neutrophils led to failure of immunotherapy. The neutrophil response depended on key components of antitumor immunity, including BATF3-dependent DCs, IL12 and IFNγ. In addition, we found that a therapy-elicited systemic neutrophil response positively correlated with disease outcome in lung cancer patients. Thus, we establish a crucial role of a neutrophil state in mediating effective cancer therapy.

Introduction

Neutrophils are the most abundant circulating leukocytes in the human body, and they accumulate in a wide range of cancer types[1–5]. A large body of evidence from mouse models indicates that tumor-infiltrating neutrophils can exhibit both tumor-promoting and antitumor functions[6]. Promotion of cancer cell proliferation, metastasis, angiogenesis and inhibition of anti-tumor T-cell responses have all been linked to neutrophils[7–12]. Nevertheless, other studies have demonstrated their capacity to directly kill cancer cells and stimulate antitumor immunity[13–18]. Much of the biological mechanisms underlying the development of these divergent functional states remain unknown[19].

Recent high-dimensional single-cell analyses have revealed that circulating and tumor-infiltrating neutrophils exhibit heterogeneity at the level of their transcriptomes and surface protein expression[20–24]. This heterogeneity raises the question of whether phenotypically distinct neutrophil states co-existing in tumors could have different, potentially opposing, functional activities and whether specific antitumor states could be therapeutically expanded. We recently showed that most neutrophil states identified in human lung tumors can also be found in mice, confirming that knowledge obtained about neutrophil heterogeneity in mouse models is highly relevant for human disease[24]. Notably, both human and mouse tumors harbor a neutrophil state characterized by high expression of interferon-stimulated genes (ISGs), yet the functional relevance of this state is not known[24].

Given the potential of cancer immunotherapies to induce durable clinical responses in some patients but not others, considerable efforts have been invested into understanding how successful immunotherapy changes the tumor microenvironment to favor tumor control. Single-cell omics studies revealed that treatments inducing successful antitumor T-cell immunity can also have an indirect effect on the myeloid compartment. This can involve the expansion of pro-inflammatory macrophages or dendritic cells that express ISGs and other immunostimulatory genes[25–28]. Despite their abundance in many tumors, neutrophils have been largely overlooked in these single-cell transcriptomics studies due to their inadvertent exclusion in standard sample preparation and analytical pipelines. Moreover, the lifespan

of neutrophils is only a few hours or days; therefore an immunotherapy-elicited neutrophil response may be missed if tumors are examined late after treatment. It is therefore largely unknown whether successful immunotherapy could have an impact on the phenotype of neutrophils in the tumor microenvironment. Investigating treatment-induced reprogramming of neutrophils could also give us clues as to whether these cells could oppose or support tumor control upon therapy.

Our current knowledge about the impact of neutrophils on immunotherapy response mostly comes from mouse experiments in which all neutrophils were sought to be depleted during therapy[29–31]. In light of the emerging evidence about the existence of diverse neutrophil states in tumors, it is conceivable that broad neutrophil depletion strategies eliminate both detrimental and beneficial neutrophil states. Hence, a deeper understanding of the factors driving the acquisition of distinct neutrophil states would allow for selective manipulation of neutrophil subpopulations. This in turn would enable us to gain a more nuanced picture of the role of neutrophils in immunotherapy.

In the current study, we aimed to address these knowledge gaps by examining how immunotherapy shapes the neutrophil compartment in mouse tumor models and how treatment-induced reprogramming of neutrophils could influence tumor control.

Results

Neutrophils accumulate in tumors in the context of successful therapy

To examine neutrophil responses after cancer therapy, we initially investigated an orthotopic mouse lung adenocarcinoma model in which tumor cells carrying the oncogenic G12D Kras mutation and lacking P53 are injected intravenously. The so-called KP tumors that develop in the lungs recapitulate key features of human lung adenocarcinomas, and show resistance to treatment with immune checkpoint inhibitors[9,24,32–35]. However, here we found that treatment with a CD40 agonist antibody led to a significant reduction in tumor burden (Fig. 1A–B).

This gave us an opportunity to study neutrophil responses in the context of an immunotherapy capable of curbing lung tumor progression. Specifically, we examined tumors early after initiation of treatment to identify potential changes in neutrophil abundance or phenotype that could contribute to early phases of the antitumor response. Two days after treatment, we found that the number of neutrophils increased more than two-fold in the lungs (Fig. 1C).

These data indicated that aCD40 treatment-induced control of KP tumors was associated with a neutrophil response. We wished to establish whether a comparable response could be observed in other tumors and immunotherapies. We therefore used the MC38 tumor model, which responded both to aCD40 treatment (Fig. 1D) and aPD-1 treatment (Fig. S1A), as expected[36–38]. Similar to our findings in the KP model, the number of neutrophils increased in MC38 tumors two days after treatment with aCD40 as seen by flow cytometry (Fig. 1E), and independently by singe-cell RNA sequencing (scRNAseq) analysis of $CD45^+$ cells (Fig 1F). Similarly, treatment of MC38 tumors with the aPD-1 antibody led to an increase in

neutrophil frequency as seen by scRNAseq (Fig. 1G) and independently by flow cytometry (Fig. S1B).

We next sought to define whether the neutrophil response could be observed in the context of other therapies. To this end, we treated KP tumor-bearing mice with three distinct therapeutic approaches: paclitaxel combined with carboplatin (pac+carbo), oxaliplatin combined with cyclophosphamide (oxa+cyc), or anti-PD1 combined with anti-CTLA4 (aPD1+aCTLA4). We have previously found that pac+carbo or aPD1+aCTLA4 treatment are largely ineffective in controlling KP lung tumor growth, whereas oxa+cyc treatment triggers immunogenic cancer cell death leading to T cell-mediated tumor control[35]. We found that oxa+cyc treatment induced a neutrophil response, whereas pac+carbo or aPD1+aCTLA4 treatment did not (Fig. 1H, Fig. S1C–E). Taken together, these data suggest that neutrophil accumulation can occur in different tumor types and is a common feature of treatments with the ability to control tumor growth (Fig. 1H).

States of immunotherapy-elicited neutrophils in KP tumors

To define the identity of neutrophils that accumulate in tumors upon immunotherapy, we performed scRNAseq combined with multiplexed surface protein profiling on $CD11b^+$ cells isolated from the lungs of healthy mice, untreated KP tumor-bearing mice, and aCD40-treated KP tumor-bearing mice (N= 42,007 cells total).

We used our prior published work in mouse KP tumors[24] as a reference to annotate cells and interpret changes in neutrophil abundance and gene expression. A total of N=30,468 cells were identified as neutrophils. In untreated KP tumors, neutrophils exist in a continuum of states that we had previously partitioned into six states (originally termed N1-N6). For the present analysis we discerned an additional, seventh, neutrophil state by partitioning the N1 state into two states (Fig. 2A–B, Table S1). We now refer to these as N1a and N1b to facilitate cross-comparison between studies (Fig. 2A–B, Fig. S2A, Table S1). This was done in order to reduce errors in identifying orthologous neutrophil states between untreated and immunotherapy-treated conditions, and also proved useful in precisely describing the changes in heterogeneity that occurred after immunotherapy.

The seven neutrophil states that we observed could be grouped into three higher-level clusters, which we named *Sell*^{hi} (comprising N1a, N1b and N2), *Cxcl3*^{hi} (comprising N3), and *Siglecf*^{hi} (comprising N4, N5 and N6) (Fig. 2B, C, Fig. S2B). *Sell*^{hi} neutrophils were detected in all experimental conditions tested including healthy tissues, whereas *Siglecf*^{hi} neutrophils as well as *Cxcl3*^{hi} neutrophils were only found in tumor-bearing tissues (Fig. 2A), confirming previous findings[24].

Using DNA-tagged TotalSeq antibodies[39], we evaluated whether neutrophil immunophenotype was consistent with mRNA expression in the KP tumor model. As a control, TotalSeq revealed that all seven neutrophil states expressed the canonical neutrophil marker Ly6G, even though *Siglecf*^{hi} neutrophils expressed very low levels of *Ly6g* mRNA (Fig. 2D). We then examined the proteins CD62L and SiglecF, which are encoded by transcripts *Sell* and *Siglecf*, respectively. These proteins were expressed across the neutrophil states in the same pattern as their transcripts in KP tumors, defining

CD62L^{hi}/SiglecF^{lo} (*Sell*^{hi}), CD62L^{lo}/SiglecF^{lo} (*Cxcl3*^{hi}), and CD62L^{lo}/SiglecF^{hi} (*SiglecF*^{hi}) clusters in the TotalSeq data (Fig. 2D). Significantly, we previously identified SiglecF expression to distinguish a neutrophil sub-population with pro-tumor functions in mouse lung tumors[9,40]. Thus, these results now link scRNAseq-defined states to previously-defined neutrophil immunophenotypes. Examining the expression of 17 additional surface markers using TotalSeq did not identify markers or marker combinations that were specific for a given neutrophil state among the N1-N6 states (Fig. S2C, D), but future high-dimensional surface protein analyses may be able to do so.

A subset of *Sell*^{hi} neutrophils expands in the context of successful immunotherapy

Considering the neutrophil states defined above, we found that the total increase in neutrophil counts observed after aCD40 treatment was attributed to only some of the states (Fig 3A). aCD40 caused a greater than 10-fold increase in the abundance of both N1a (*Sell*^{hi} *Ngp*^{hi}) and N2 (*Sell*^{hi} *Cxcl10*^{hi}) neutrophils, whereas the number of N1b (*Sell*^{hi} *Lst*^{hi}), N4 (*Siglecf*^{hi} *Xbp1*^{hi}), N5 (*Siglecf*^{hi} *Ccl3*^{hi}) and N6 (*Siglecf*^{hi} *Ngp*^{hi}) cells remained unchanged. The N3 (*Cxcl3*^{hi}) neutrophil state seemingly disappeared; yet genes marking this state (e.g. *Wfdc17, Tgm2, Gos2*) did not vanish but became broadly expressed by N1b (*Sell*^{hi} *Lst*^{hi}) and N2 (*Sell*^{hi} *Cxcl10*^{hi}) neutrophils (Fig. S3A, B). These observations were supported independently by flow cytometry: aCD40 treatment led to an increase in tumor-infiltrating SiglecF^{lo}, but not SiglecF^{hi}, neutrophils (Fig. 3B), confirming that immunotherapy-elicited neutrophils are distinct from SiglecF^{hi} tumor-promoting neutrophils. Of note, CD62L had insufficient discriminatory power for separating these neutrophil subsets via flow cytometry, and rather displayed a continuum of expression, possibly due to loss of the protein over extended tissue residence (Fig. S3C).

Nevertheless, we could confirm treatment-induced expansion of SiglecF^{lo} cells with high CD62L expression (Fig. S3C). Additionally, TotalSeq revealed that SiglecF^{lo} neutrophils showed increased CD14 expression after aCD40 treatment (Fig. S2C, D), which we confirmed by flow cytometry (Fig S3D).

We wished to establish whether comparable changes in neutrophils occur in other contexts and models of immunotherapy. To investigate this question, we first performed a meta-analysis of scRNAseq datasets from KP and MC38 tumors treated with aPD1 or aCD40 to define orthologous states between these experimental conditions (Fig. 3C, left). We compared cell states obtained from different studies and experimental conditions by defining a reciprocal similarity score between states, analogous to recriprocal similarity commonly used to identify orthologous genes[41,42], and which we have previously employed to identify orthologous dendritic cell states[43]. This analysis revealed that five of the transcriptional states we identified in the current study were conserved in KP and MC38 tumors as well as in aCD40 and aPD1 treatments (Fig. 3C, right). Notably, all *Sell*^{hi} neutrophil states overall showed high conservation of their transcriptome between aCD40-treated KP tumors and aCD40- or aPD1-treated MC38 tumors. In comparison, the *Cxcl3*^{hi} state showed the poorest conservation both across tumors and between treatments, which is consistent with the lack of stability of this state upon treatment in KP lung tumors noted above.

We then examined changes in the abundances of orthologous states (Fig. 3D). Significantly, as with aCD40 treatment in KP tumors, the scRNAseq of MC38 tumors showed an increase in neutrophil abundance after both aCD40 and aPD1 treatments in clusters orthologous to the KP tumor *Sell*^{hi} clusters. Altogether these results indicate that several of the neutrophil states we observe in lung tumors appear to represent stereotyped responses, as are the changes in neutrophils associated with therapies that trigger effective anticancer adaptive immunity.

Neutrophils elicited by immunotherapy acquire an interferon-stimulated gene signature

Having established that aCD40 treatment triggered intratumoral accumulation of *Sell*^{hi} *(Siglecf*^{lo}*)* but not *Siglecf*^{hi} *(Sell*^{lo}*)* neutrophils, we sought to understand how such changes might correlate with or affect successful anti-tumor responses. To explore possible hypotheses, we asked whether the neutrophil subsets differ in the expression of genes associated with pro- and anti-tumoral activity, or whether therapy might modulate such genes within the cell subsets. Using scRNAseq data, we first examined the expression of genes previously linked to angiogenesis, extracellular matrix (ECM) remodeling, immunosuppression, tumor proliferation, and/or myeloid cell recruitment (Fig 4A). All of these pro-tumor signatures showed higher expression in *Siglecf*^{hi} neutrophils compared to *Sell*^{hi} neutrophils (Fig. 4A). Interestingly, aCD40 treatment modulated genes associated with tumor proliferation and myeloid cell recruitment in *Siglecf*^{hi} cells (Fig. 4B). In contrast, the genes associated with cytotoxic activity as well as a large set of ISGs were enriched in *Sell*^{hi} neutrophils (Fig. 4C), and aCD40 treatment led to further induction of these genes in *Sell*^{hi} cells (Fig. 4D, E).

To confirm the induction of an ISG phenotype by neutrophils upon aCD40 treatment, we used reporter mice for CXCL10, a prototypical ISG[44]. Flow cytometry analysis of CXCL10-BFP reporter expression revealed that aCD40 treatment in KP tumors indeed led to robust CXCL10 induction, specifically in tumor-infiltrating SiglecF^{lo} neutrophils (Fig 4F). CXCL10 expression could be observed in 40% of SiglecF^{lo} neutrophils and was restricted to CD14^{+} cells (Fig. S4A, B).

We examined data from murine MC38 tumors and human non-small cell lung cancer (NSCLC) to evaluate whether induction of this ISG response could be recapitulated in other contexts. Indeed, the increased ISG signature was also seen in *Sell*^{hi} neutrophils in the MC38 tumor model and was elevated in the same cell state in this model in response to both aCD40 and aPD1 immunotherapy (Fig. 4G). Furthermore, among human neutrophils identified as analogous to the *Sell*^{hi} populations[24], we observed the same pattern in ISGs as among the murine subsets found in untreated KP tumors (Fig. 4G). In addition, flow cytometry revealed an increase in CXCL10-BFP^{+} neutrophils in MC38 tumors after aCD40 treatment (Fig. 4H). IFNγ neutralization reduced expression of CXCL10 in these neutrophils, supporting the notion that IFNγ is a key factor in inducing ISGs (Fig. 4I).

Taken together, these results show that aCD40 treatment induces the expression of ISGs in *Sell*^{hi} *(Siglecf*^{lo}*)* neutrophils, and that ISG-expressing neutrophils are highly conserved across different tumor types and immunotherapies.

Immunotherapy-elicited neutrophils show a distinct phenotype and maturation state

Neutrophils are typically short-lived, with a half-life of a few hours or days[6,45,46]. Changes in the abundance and gene expression of neutrophils could therefore arise locally in the tumor, or they may reflect changes during neutrophil maturation. Since neutrophils originate in the bone marrow and transit through the blood, we sampled these sites for neutrophils after aCD40 treatment. After treatment, we found that some neutrophils in the blood, and even the bone marrow, already showed increased CXCL10-BFP expression upon therapy (Fig. 5A). Circulating neutrophils also showed increased production of reactive oxygen species (ROS) (Fig. 5B). This suggested that in response to aCD40 treatment, neutrophils can begin acquiring features of the ISG phenotype before they reach the target site.

This led us to ask whether ISG-expressing *Sell*^{hi} neutrophils stimulated by aCD40 might have a different origin than *Siglecf*^{hi} neutrophils, which do not show a comparable response to treatment. Both *Sell*^{hi} and *Siglecf*^{hi} neutrophils contain a subset enriched in *Ngp*, a transcript expressed during neutrophil maturation[47]. It is therefore possible that N1a (*Sell*^{hi} *Ngp*^{hi}) and N6 (*SiglecF*^{hi} *Ngp*^{hi}) neutrophils are distinct precursors, which give rise to other *Sell*^{hi} and *Siglecf*^{hi} states respectively. This hypothesis is consistent with two further observations. First, we examined the expression of a broader set of genes associated with early or immature neutrophils, defining a composite “neutrotime” gene expression score[47]. We found that N1a (*Sell*^{hi} *Ngp*^{hi}) and N6 (*Siglecf*^{hi} *Ngp*^{hi}) neutrophils displayed the lowest “neutrotime” among the seven neutrophil states (Fig. 5C, D). Thus, these states expressed multiple transcripts associated with less mature cells. Second, we calculated “RNA velocities” to identify trajectories on scRNAseq UMAP plots[48,49]. Applying this approach to our dataset (Fig. 5E), two consistent trajectories were predicted under all conditions examined. The first ranged from N1a (*Sell*^{hi} *Ngp*^{hi}), to N1b (*Sell*^{hi} *Lst*^{hi}), to N2 (*Sell*^{hi} *Cxcl10*^{hi}) neutrophils; the second ranged from N6 (*Siglecf*^{hi} *Ngp*^{hi}) to N4 (*Siglecf*^{hi} *Xbp1*^{hi}) neutrophils (Fig. 5E, Fig. S5A). Thus, the RNA velocity data are also consistent with the possibility that neutrophils can undergo two distinct state transition trajectories in tumors.

Since the number of N1a (*Sell*^{hi} *Ngp*^{hi}) neutrophils increased sharply after aCD40 treatment, we considered that this treatment recruited incompletely mature SiglecF^{lo} neutrophils to the tumor. Accordingly, we observed reduced expression of maturity markers[50,51] (CD101, CD11b, Ly6G) on SiglecF^{lo} neutrophils, but not on SiglecF^{hi} neutrophils, upon treatment (Fig. 5F). Among SiglecF^{lo} neutrophils, CD62L^{hi} cells appeared slightly less mature compared to CD62L$^{int/lo}$ cells (Fig. S5B). Morphological analysis further confirmed appearance of immature cells with lower nuclear segmentation within the SiglecF^{lo} population upon treatment. At the same time, the SiglecF^{hi} population remained unaffected and showed a mature morphology with highly segmented nuclei (Fig. 5G,H)[46,52]. It has been recently reported that immature neutrophils can be identified in tissues as MPO^{hi}Ly6G^{lo} cells using immunofluorescent staining of tissue sections[53]. Indeed, we observed increased infiltration of MPO^{hi}Ly6G^{lo} cells into KP lung tumors following aCD40 treatment, while the density of MPO^{hi}Ly6G^{hi} cells remained the same (Fig. S5C).

Finally, we asked whether stimuli other than aCD40 could trigger a similar neutrophil response. We found that LPS treatment, but not type I/II interferon or poly-IC, induced

appearance of $CD14^{+}CD101^{-}$ neutrophils in the periphery, similar to aCD40 treatment (Fig. S5D). Taken together, these data demonstrate that aCD40-elicited neutrophils enter the tumor in a different state than $SiglecF^{hi}$ neutrophils: they already exhibit an interferon response and increased ROS production, they are less mature than $SiglecF^{hi}$ neutrophils, and they resemble neutrophils that emerge during systemic bacterial infections[54].

A neutrophil IRF1-mediated interferon response is required for tumor control

Next, we asked whether neutrophils were required for tumor control in the context of aCD40 treatment. Therapy-elicited neutrophils were able to induce IL12 production in DCs and kill cancer cells *in vitro*, suggesting their potential immunostimulatory and cytotoxic activity (Fig. S6A, B). To study the role of therapy-elicited neutrophils *in vivo*, we used the MC38 tumor model, in which aCD40 treatment triggered the highest increase in neutrophil abundance among all the conditions examined (Fig. 1H). The neutrophils infiltrating MC38 tumors after aCD40 treatment showed the same increase in CD14 and loss of CD101 as in the KP model (Fig. 6A) and highly expressed CXCL10, a marker of the ISG response (Fig. 4H, Fig. 6A).

We first considered non-specifically depleting neutrophils using anti-Ly6G monoclonal antibodies - a method that is widely used but has been recently reported to have limited efficacy particularly in depleting immature neutrophils[29]. Indeed, we found that 28% of neutrophils remained in MC38 tumors after treatment with anti-Ly6G (Fig. S6C, D). Furthermore, the cells persisting after anti-Ly6G treatment were less mature, indicated by their lower expression of CD101 and CXCR2 as well as their higher expression of CXCR4 (Fig. S6E). As we found that a large portion of immunotherapy-elicited neutrophils had decreased levels of Ly-6G expression and were already less mature (Fig. 5C–H), anti-Ly6G treatment would likely not be suitable to completely deplete these cells.

Instead, we searched for transcription factors that could play a key role in the development of the immunotherapy-elicited neutrophil response and could be specifically targeted. We performed computational prediction of transcription factor activity based on highly enriched genes in aCD40-expanded neutrophil states (N1a and N2) versus all other states. Among the top transcription factors predicted to be active in aCD40-expanded neutrophils, we found IRF1 to be one of the highest ranked and associated with the largest regulated gene set (Fig. 6B). In addition, IRF1 expression in neutrophils increased upon aCD40 treatment (Fig. S6F) and this transcription factor has been described to regulate CXCL10 expression[55], one of the hallmarks of immunotherapy-elicited neutrophils (Fig. 3A, Fig. 4F–H, Fig. 5A). These observations prompted us to examine whether deletion of *Irf1* could prevent the emergence of aCD40-elicited ISG-responsive neutrophils. As a proxy, we again leveraged the observations that an increase in CD14 and a reduction in CD101 expression in neutrophils occurred following aCD40 treatment (Fig. 6A). Interestingly, we found that aCD40 treatment in $Irf1^{-/-}$ mice failed to induce an increase of $CD14^{+}$ $CD101^{-}$ neutrophils in MC38 tumors (Fig. 6C). Thus, targeting IRF1 expression may be used to modulate immunotherapy-elicited neutrophil responses *in vivo*.

Given these results, and to ensure that IRF1-deficiency is limited to neutrophils, we generated mixed bone marrow chimeras with 50% $Csf3r^{-/-}$ cells and 50% $Irf1^{-/-}$ cells.

Csf3r$^{-/-}$ cells are largely unable to differentiate into neutrophils, but can give rise to other lineages[17,56,57]. Hence, in *Csf3r*$^{-/-}$/*Irf1*$^{-/-}$ mixed bone marrow chimeras peripheral neutrophils originate only from *Irf1* knock-out bone marrow, while all other immune cells comprise a 50–50% mixture of *Irf1*-proficient *Csf3r*$^{-/-}$ cells and *Irf1*-deficient cells, resulting in full IRF1 loss restricted to neutrophils. Strikingly, mice with neutrophil-specific IRF1-deficiency failed to show tumor control following aCD40 treatment, contrary to mice with wild-type neutrophils (Fig. 6D). Of note, type 1 conventional DCs and CD8$^+$ T cells, two key requirements of antitumor immunity upon aCD40 treatment, did not show significantly different abundance in the tumors of WT/*Csf3r*$^{-/-}$ and *Irf1*$^{-/-}$/*Csf3r*$^{-/-}$ mixed bone marrow chimeras (Fig. S6G, H). Overall, we found that the emergence of CD14$^+$CD101$^-$ neutrophils in the tumor upon treatment required the activity of the transcription factor IRF1, and preventing treatment-induced neutrophil response by neutrophil-specific IRF1-deletion abrogated response to aCD40 immunotherapy.

Therapy-elicited neutrophil accumulation in tumors depends on key components of antitumor immunity

Given that ISG-responsive neutrophils were required for aCD40-mediated tumor control, we explored the mechanisms regulating their emergence in the tumor. We began by exploring the hypothesis that the neutrophil response in tumors depends on components that are key in the anti-cancer immune response. We and others have previously found that antitumor immunity upon aCD40 therapy relies on the presence of cDC1s, which require the transcription factor BATF3 for their differentiation. IL12, produced by DCs and other myeloid cells, is necessary for the activation of antitumor T cells, which, in turn, secrete IFNγ to amplify the antitumor immune response[36,58,59]. Specifically, in aCD40-treated MC38 tumors, we found that IL12 was produced almost exclusively by DCs and macrophages, while the IFNγ-producing cells were predominantly CD8$^+$ T cells and natural killer cells (Fig. S6I, J). CXCR3, the receptor for CXCL9/10, has been reported as another key requirement for intratumoral activation of T cells upon immunotherapy[60]. We could indeed confirm high *Cxcr3* expression primarily on T cells in aCD40-treated MC38 tumors (Fig. S6K).

To dissect the relevance of these components in the ISG neutrophil response at the tumor site, we have employed either transgenic mice or cytokine inhibitors. Interestingly, we found that *Batf3*$^{-/-}$ mice, *Il12b*$^{-/-}$ mice, wild-type mice treated with IFNγ-neutralizing mAbs or *Cxcr3*$^{-/-}$ mice all showed impaired accumulation of CD14$^+$CD101$^-$ neutrophils in MC38 tumors after aCD40 treatment (Fig. 6E). In contrast, CD14$^-$CD101$^+$ neutrophils remained largely unaffected in the same experimental models. Overall, these results indicate that key components of antitumor immunity, including BATF3-dependent DCs, IL12 and IFNγ production as well as the CXCR3 chemokine receptor, are all required for the generation of the neutrophil response upon immunotherapy.

Systemic neutrophil response in small-cell lung cancer patients is associated with better outcome following immunotherapy

Finally, we wanted to determine the relevance of a therapy-elicited neutrophil response in human disease. To this end, we analyzed data from a clinical trial in small-cell lung

cancer (NCT02046733)[61]. We focused on patients who received standard-of-care chemo-radiotherapy combined with ipilimumab (anti-CTLA4) and nivolumab (anti-PD1) immune checkpoint inhibitors (n=78). We examined the neutrophil to lymphocyte ratio (NLR) in the peripheral blood, a widely used and technically robust indicator of neutrophil-biased hematopoiesis[62]. High baseline NLR (>2.5) in treatment-naive patients correlated with worse outcome following adjuvant immunotherapy (Fig. 6F) compared to low NLR, in line with previous findings[63] (P = 0.0296, HR = 0.4712, 95% CI of HR: 0.2392–0.9282). To specifically investigate therapy-elicited neutrophil responses, we assessed changes in NLR in response to radio-chemotherapy. We compared the outcome of patients showing NLR increase upon therapy versus baseline (>10% increase, n=54) with patients showing NLR decrease (>10% decrease, n=16). Interestingly, patients with therapy-induced increase in NLR experienced significantly better progression-free survival following adjuvant immunotherapy than patients with decreased NLR (P = 0.0292, HR = 0.4635, 95% CI of HR: 0.2323–0.9251) (Fig. 6G). Overall, these results indicate that a therapy-elicited systemic neutrophil response can positively correlate with disease outcome in lung cancer patients.

Discussion

By detailing the complexity of neutrophils in the context of therapy in mice, this study reveals that the responses mediated by these cells are heterogeneous but stereotyped, and include states with critical antitumor effects. We believe these results are important because they reconcile previous findings that revealed pro-tumor or anti-tumor effects for neutrophils when these cells were studied as a single population[19].

The transcription factor IRF1 has been described as an enhancer of the ISG response and a modulator of cytokine and chemokine expression in both epithelial cells and DCs[55,64]. The role of IRF1 in neutrophils remains less studied; however, the IRF1 binding motif is highly enriched in the open chromatin regions of granulocyte-monocyte progenitors after beta-glucan treatment, and these progenitors give rise to neutrophils that have potent antitumor activity[65]. These observations, along with the results of the present study, indicate that IRF1 may be a critical upstream regulator of antitumor neutrophil production. The results presented here also suggest that pro- and antitumor neutrophils coexist within tumors without differentiating from each other, but rather likely to have distinct origins. From a therapeutic perspective, it is possible that reprogramming tumor-associated neutrophils may be less effective in controlling tumors than selectively increasing antitumor neutrophils and/or depleting protumor neutrophils. It will therefore be important to define the mechanisms that dictate the fate of neutrophil progenitors and how they can be harnessed for therapeutic purposes.

Since antitumor neutrophils have high cytotoxic potential and expand systemically upon treatment, there must be regulatory mechanisms that ensure that these cells perform their functions only within the target sites. It is interesting to note that the deployment of the neutrophilic response at the tumor site is strictly dependent on IL12, DCs, and IFNγ, which are molecular and cellular factors present in tumors and are part of a positive feedback loop necessary for the local promotion of antitumor T-cell responses[36]. Accordingly, we did

not observe a neutrophil response in KP tumors following anti-PD1 therapy, which fails to induce antitumor T-cell immunity in this model[35]. In contrast, anti-PD1 elicited a neutrophil response in MC38 tumors, in which T cells can be activated by this treatment[36]. It is also conceivable that T-cell mediated tumor cell killing and subsequent release of danger signals contributes to neutrophil mobilization and infiltration into the tumor. Furthermore, IL-12$^+$ DCs are found directly adjacent to blood vessels in the tumor stroma[66], and should therefore be able to interact effectively with neutrophils entering the tumor to allow them to exert their effector functions locally. It should also be noted that IL-12 and IFNγ production occur in healthy tissue in the context of immunotherapy-related adverse events, which triggers a tissue destructive neutrophil response[59]. Taken together, these data suggest that IL-12 and IFNγ signaling are required to promote cytotoxic neutrophil responses, and that these responses can occur in many different tissues. Neutrophil expansion with an ISG signature has also been described after myocardial infarction or various infections[54,67–69]. Therefore, ISG-expressing neutrophil states that develop after immunotherapy could be analogous to neutrophils with tissue-destroying and immunostimulatory activity described in other pathological contexts.

It is likely that neutrophils stimulated by immunotherapy exhibit different antitumor functions. For example, previous work has indicated that neutrophil production of H_2O_2 [70,71] or granular enzymes, including neutrophil elastase[13] and cathepsin-G[72], may have tumoricidal effects. Neutrophils may also support adaptive immunity, for example by promoting antigen release through cancer cell killing. Also, some tumor-associated neutrophils upregulate costimulatory molecules and can cross-present antigens to CD8$^+$ T cells[16,18,73]. The high expression of CXCL10 by antitumor neutrophils could also promote interactions with CXCR3-expressing T cells to drive antitumor immunity. The importance of neutrophil-T cell interactions is illustrated by the observation that enrichment of CD4$^+$ PD-1$^+$ T cells in granulocyte-dominated cell neighborhoods is associated with a favorable prognosis in colorectal cancer[4]. Also, some of the characteristics of immunotherapy-stimulated neutrophils that we have defined here have been described as markers of antitumor neutrophils in previous studies. For example, a subset of immunostimulatory neutrophils identified in early human lung cancer lesions was characterized by CD14 expression and required IFNγ for expansion[18]. It is possible that CD14/TLR4 signaling directly contributes to neutrophil reprogramming because Myd88, downstream of TLR4, is required for the acquisition of the antitumor neutrophil phenotype in mouse uterine carcinomas[74]. Finally, we found that *Sell*^{hi} neutrophils in KP tumors expressed elevated levels of CXCL10 in response to immunotherapy, which is similar to tumoricidal neutrophils that can emerge after TGFb neutralization in mice[14,75].

Overall, our study demonstrates that neutrophils exhibit remarkable plasticity and can acquire an antitumor phenotype in response to immunotherapy. Although the treatment-induced neutrophil response may be short-lived, neutrophils could support the induction of a long-term adaptive immune response. Therefore, cancer immunotherapy approaches that induce antitumor T-cell immunity in combination with therapies that optimally engage, rather than deplete, antitumor neutrophils could lead to more durable tumor control after treatment.

Limitations of the study

In this study, we first draw attention to a limitation of the mixed bone marrow chimera technique used to assess the requirement of IRF1 in neutrophils. In this experiment, it is assumed that *Csf3r*$^{-/-}$ and *Irf1*$^{-/-}$ cells can engraft equally and that peripheral neutrophils originate only from *Irf1* knock-out bone marrow, whereas all other immune cells comprise a 50–50% mixture of *Irf1*-proficient *Csf3r*$^{-/-}$ cells and *Irf1*-deficient cells. Thus, it is expected that up to 50% of non-neutrophil immune cells will carry a loss of IRF1, and the remaining 50% of IRF1-proficient cells will be sufficient to maintain a functional response. In future studies, the generation of conditional neutrophil-specific IRF1 knockouts should further define the function of this transcription factor in the context of cancer immunotherapy. Second, the data presented in this study do not define the mechanisms by which neutrophils contribute to tumor control. The generation of neutrophil-specific conditional knockouts of candidate genes potentially involved in tumor control could help answer this question. Third, our human studies suggest the importance of revisiting NLR as a dynamic readout with prognostic potential. This will require prospective investigations in a larger patient population.

STAR★METHODS

RESOURCE AVAILABILITY

Lead contact—Further information and requests for resources or reagents should be directed to and will be fulfilled by the Lead Contact: Mikael J. Pittet (mikael.pittet@unige.ch).

Materials availability—This study did not generate new unique reagents.

Data and code availability

- Single-cell RNA-seq data have been deposited at GEO and are publicly available as of the date of publication. Accession numbers are listed in the key resources table. Microscopy and flow cytometry data reported in this paper will be shared by the lead contact upon request.
- All original code has been deposited at GitHub and is publicly available as of the date of publication. The link is listed in the key resources table.
- Any additional information required to reanalyze the data reported in this paper is available from the lead contact upon request.

EXPERIMENTAL MODEL AND SUBJECT DETAILS

Cell lines—KP1.9 cells, derived from lung tumor nodules of a male C57BL/6 KP mouse were obtained from Alfred Zippelius (University Hospital Basel, Switzerland). KP1.9 cells were maintained in IMDM medium supplemented with 10% fetal bovine serum and 1% penicillin/streptomycin. MC38 cells (obtained from Mark J. Smyth) and MC38-H2B-GFP cells (obtained from Ralph Weissleder), both derived from a female mouse, were maintained in DMEM medium supplemented with 10% fetal bovine serum and 1% penicillin/streptomycin.

Mice—Animals were bred and housed under specific pathogen free conditions at the Massachusetts General Hospital and at the Agora Cancer Research Center. Experiments were approved by and were performed in accordance with the animal care and use committees of MGH, University of Geneva and canton Vaud. C57BL6/J mice (Cat #000664), *Batf3*$^{-/-}$ (Cat #013755), *Il12p40*$^{-/-}$ (Cat #002693), IL-12p40-IRES-eYFP (Cat #006412), *Csf3r*$^{-/-}$ (Cat #017838), *Irf1*$^{-/-}$ (Cat #002762), IFNg-IRES-eYFP (Cat #017581) were all obtained from Jackson Laboratories. Kras$^{LSL\text{-}G12D/+}$;Trp53$^{flox/flox}$ mice were from the lab of Tyler Jacks (MIT, Boston, USA) and maintained in our facility. REX3-Tg and *Cxcr3*$^{-/-}$ mice were received from the lab of Andrew D. Luster (MGH, Boston, USA) and maintained in our facility. 7–14 week old mice were used for experiments. Male mice were used for experiments involving the KP1.9 tumor model. Both male and female mice were used for all other experiments and experimental groups were sex-matched.

METHODS DETAILS

Mouse tumor models—KP lung tumors were induced by intravenous tail vein injection of 2.5 x 10^5 KP1.9 cells into male C57BL6/J mice, as described previously[9,35]. KP1.9-derived tumors were allowed to grow for two weeks prior to aCD40 therapy. For assessing tumor control by aCD40, on day 14 of tumor growth tumor-bearing mice were treated with 5 mg/kg of aCD40 (clone FGK4.5, BioXCell Cat #BE0016-2) intraperitoneally. These mice were then euthanized between 33–35 days after tumor induction, and tumor burden was assessed by measuring post-mortem lung weight and by histological analysis using hematoxylin and eosin (H&E) staining. For experimental readouts assessing neutrophil responses, aCD40 was given two days before endpoint (typically day 33).

For chemotherapy or aPD1+aCTLA4 treatment experiments, KP lung tumors were induced by intratracheal (i.t.) delivery of Adenovirus-Cre (AdCre) to Kras$^{LSL\text{-}G12D/+}$;Trp53$^{flox/flox}$ mice, as described previously[9,35]. Tumor-bearing mice were treated once a week for 3 weeks, with intraperitoneal injections of 10 mg/kg of paclitaxel combined with 10 mg/kg of carboplatin, or 2.5 mg/kg of oxaliplatin combined with 50 mg/kg of cyclophosphamide, as described previously[35]. Treatments with a combination of aPD-1 (clone 29F.1A12, 200 μg/mouse, provided by Dr. G. J. Freeman) and aCTLA-4 (clone 9D9, 100 μg/mouse, BioXCell) were performed as described previously[35]. Mice were euthanized 3 days after the last treatment, and tumor burden was assessed by histological analysis using hematoxylin and eosin (H&E) staining.

MC38 cells were implanted at 2 x 10^6 cells per tumor in the flank subcutaneously. Tumor-bearing mice were treated with 5 mg/kg of aCD40 on day 7 of tumor growth. Tumor size was recorded over time with a digital caliper and tumor volumes were calculated as:

$$Volume = \pi/6 \; x \; length \; x \; width^2$$

Experimental readouts assessing neutrophil responses were performed two days following aCD40 treatment. Experimental readouts assessing $CD8^+$ T cells and DCs were performed seven days following aCD40 treatment. For aPD-1 treatments, tumor-bearing mice were treated with 200 μg of aPD-1 when MC38 tumors reached approximately 75mm^3,

as described previously[36]. Neutrophil response readouts were performed 2 days after treatments.

Flow cytometry and cell sorting—KP tumor-bearing lungs were perfused post-mortem by PBS injection through the right ventricle of the heart. MC38 tumors and KP tumor-bearing lungs were isolated and minced using surgical scissors, then digested with 0.2 mg/ml Collagenase I (Worthington) in RPMI-1640 at 37C for 30 minutes shaking at 900 rpm. Digested tissues were then processed through a 40 μm cell strainer, centrifuged at 1500 RPM for 5 minutes, subjected to red blood cell lysis for 1 minute using ACK lysis buffer, and resuspended in PBS with 0.5% BSA for staining. For blood analyses, 5 ul blood was diluted in 1 ml of PBS with 2mM EDTA and 0.5% FBS. Red blood cells were lysed using ACK lysis buffer for 5 minutes and resuspended in PBS with 0.5% BSA for staining. For bone marrow analyses, femurs were harvested and bones were flushed using a 26-g needle with 0.5% BSA in PBS until bones appeared white. Harvested cells were processed through a 40 μm cell strainer, subjected to ACK lysis for up to 5 minutes and resuspended in PBS with 0.5% BSA for staining. Cell suspensions were stained with Zombie Aqua or Zombie Green or 7-AAD (Biolegend) to exclude dead cells, incubated with Fc Block TruStain FcX (Clone 93, Biolegend) in PBS with 0.5% BSA, and then stained with fluorochrome labeled antibodies (listed in the Key Resources Table). Cells were quantified using Precision Count Beads (Biolegend). ROS production was assessed using the CellROX Green reagent (Invitrogen). Cells were resuspended in DMEM and incubated with the CellROX Green reagent for 30 min at 37°C. After washing the cells with PBS, cells were stained for flow cytometry as described above. Samples were run on a BD LSR II flow cytometer and analyzed using FlowJo software (Treestar). Cell sorting was performed using a BD FACS Aria II sorter.

Histology—KP tumor-bearing lungs were perfused post-mortem by PBS injection through the right ventricle of the heart. Then lungs were excised and placed in ice cold PBS. Tissues were fixed in either 10% formalin overnight, then washed twice with PBS and placed in 70% Ethanol or PBS until processing, or 4% paraformaldehyde and then cryoprotected in sucrose overnight and embedded in OCT for freezing. For H&E, tissues were paraffin embedded, sectioned, and stained with Hematoxylin and Eosin at the MGH Histopathology Research Core.

Paraffin-embedded sections were deparaffinized and rehydrated prior to immunohistochemical staining. Heat induced antigen retrieval was performed using Retrievagen A (pH6.0) (550524, BD Biosciences), and the sections were permeabilized with 0.3% Triton X-100 in PBS for 10 minutes at room temperature. After the sections were blocked with 4% normal rabbit serum in PBS for 1 hour at room temperature, a primary antibody, Ly6G (clone 1A8, BioLegend, 127602, 1:25) was incubated at 4°C overnight. A biotinylated rabbit anti-rat IgG secondary antibody (Vector Laboratories, BA-4001, 1:100) was applied, and VECTASTAIN ABC-HRP kit (Vector Laboratories, PK-6100) and AEC Substrate (Agilent, K3469) were used for the detection. Nuclei were counterstained with Harris Hematoxylin (Sigma, HHS32) and all the images were captured by using a digital scanner NanoZoomer 2.0RS (Hamamatsu, Japan). For immunofluorescent

staining, strepravidin DyLight 594 (Vector Laboratories, SA-5594, 1:600) was used after a biotinylated rabbit anti-rat IgG and nuclei were stained with DAPI (ThermoFisher Scientific, D21490). The number of $Ly6G^+$ cells was determined manually and normalized to the area of the field of view.

Frozen lung tissues were permeabilized for 10 minutes in 0.1% Triton X-100 in PBS 1x. After 30 minutes blocking in 1% BSA in PBS, primary Ly6G (clone 1A8, BioLegend, 127602, 1:100) and MPO (R&D systems, AF3667, 1:200) antibodies were applied on 10um sections and incubated overnight at 4°C. Secondary antibodies, donkey anti-goat Alexa 647 (ThermoFisher Scientific, A21447, 1:1000) and goat anti-rat Alexa568 (ThermoFisher Scientific, A11077, 1:1000) were incubated sequentially for 45 minutes each. Sections were counterstained with DAPI (ThermoFisher Scientific, D21490) and mounted with FluoromountG (Bioconcept, 0100–01). All the images were captured by using a digital scanner Axioscan 7 (Zeiss).The numbers of $MPO^{hi}Ly6G^{hi}$ and $MPO^{hi}Ly6G^{lo}$ cells were determined by manual counting in tumor areas and were normalized to the area of the field of view.

MC38 tumors were formalin fixed and paraffin embedded as described above. Sections were then stained using the Ventana Discovery ULTRA automate (Roche Diagnostics). All steps were performed automatically with Ventana Solutions, unless otherwise noted. The dewaxed and rehydrated paraffin sections were heat pre-treated using CC1 solution for 40 min at 95°C. Primary antibody was applied and revealed with anti-rat Immpress HRP (Ready to use, Vector Laboratories) followed by incubation with Cy5 fluorescent tyramide. The primary antibody was rat anti-CD8 (clone 4SM15, ThermoFisher Scientific, 14–0808-82, 1:100) Sections were counterstained with DAPI (ThermoFisher Scientific, D21490) and mounted with FluoromountG (Bioconcept, 0100–01). All the images were captured by using a digital scanner Axioscan 7 (Zeiss). The fraction of $CD8^+$ cells within all $DAPI^+$ cells was determined in cross-sections of entire tumors using an automated cell classifier in QuPath.

Quantification of neutrophils following different therapies—In Fig. 1H, neutrophil quantification is shown based on flow cytometry (KP+aCD40; MC38+aCD40; MC38+aPD1) or immunofluorescence staining of Ly6G in tissue sections (KP+aPD1/aCTLA4; KP+Oxa/Cyc; KP+Pac/Carbo).

Cytospin—$SiglecF^{hi}$ and $SiglecF^{lo}$ neutrophils were sorted from lung tissue of KP tumor-bearing mice with or without aCD40 treatment. Cytospins were performed using a Shandon Cytospin 4 centrifuge (Thermo Fisher Scientific). In detail, 10^5 cells were centrifuged (700 rpm, 5 min) onto Tissue Path Superfrost Plus Gold microscope slides (ThermoFisher Scientific) and dried overnight at room temperature. Cells were then fixed in 4% formaldehyde-buffered solution and stained with hematoxylin and eosin (H&E) using the ThermoScientific Shandon Varistain Gemini ES Automated Slide Stainer. Slides were scanned using Axioscan 7 (Zeiss). The number of nuclear lobes was counted manually on at least 50 cells per condition.

Cytokine neutralization—Neutralization of IFNγ was performed by intraperitoneal injection of 1 mg of anti-IFNγ (Clone XMG1.2, BioXCell Cat# BE0055) initially on day 7

of tumor growth, with an additional 500 μg of anti-IFNγ dosed on day 8, then mice were analysed on day 9.

Anti-Ly6G treatment—Anti-Ly6G (BioXCell Cat #BP0075) was administered at 500 μg / mouse on day 7 (−2h before aCD40) and boosted with 250 μg/mouse on day 8, then mice were analysed on day 9.

LPS, IFNβ, IFNγ, polyI:C treatments—Mice were treated by intraperitoneal injection with 5 mg/kg of LPS (Invivogen, tlrl-eblps), 5 x 10^6 U/kg of recombinant mouse IFN-β1 (BioLegend, Cat# 581302), 7.5 x 10^5 U/kg of recombinant murine IFNγ (Peprotech, Cat# 315–05) or 5 mg/kg of polyI:C (Invivogen, tlrl-pic). Experimental readouts assessing neutrophil responses were performed two days following these treatments.

Bone marrow chimeras—C57BL6/J recipient mice (Cat #000664) were irradiated with a single dose of 1000 cGy using a cesium-137 irradiator. The next day, bone marrow was harvested from donor mice, including WT C57BL6/J mice (Cat #000664), *Csf3r*$^{-/-}$ mice (Cat #017838), or *Irf1*$^{-/-}$ mice (Cat #002762). Cells from each type of donor were counted manually. For 50:50 bone marrow chimeras, cells were mixed at a 1:1 ratio before injection. Cells were injected retro-orbitally at 10–14 x 10^6 total cells / mouse in 200–400 μL volume, and mice were allowed to reconstitute for 5.5–7.5 weeks.

***In vitro* co-cultures—**Two days after aCD40 treatment, livers were excised and digested with 450 U/ml collagenase I, 125 U/ ml collagenase XI, 60 U/ml DNase I, 60 U/ml hyaluronidase (Sigma Aldrich), and 20 mM HEPES buffer in PBS at 37°C for 20 minutes shaking at 900 rpm, as described previously[59]. Digested tissue was then processed through a 40 μm cell strainer, centrifuged at 1500 rpm for 5 minutes, subjected to ACK red blood cell lysis, and resuspended in PBS with 0.5% BSA. Magnetic selection with anti-Ly-6G microbeads (Miltenyi Biotec) was used to isolate neutrophils from the resulting cell suspension. Isolated neutrophils were co-cultured with MC38-H2B-GFP tumor cells (40:1 neutrophil:cancer cell ratio). GFP$^+$ tumor cells were quantified 24 hours later via microscopy (DeltaView). Co-culture of cancer cells with splenocytes from untreated mice was used as a negative control condition. For DC/neutrophil co-cultures, bone marrow cells were isolated from IL-12p40 reporter (IL12p40-eYFP) mice and cultured with 300 ng/mL Flt3L (Peprotech) for 8–10 days to generate DCs. Neutrophils were co-cultured with DCs (10:1 neutrophil:DC ratio) for 24 hours, before quantifying YFP$^+$ cells via microscopy (DeltaVision). Treatment with TLR7/8 agonist R848 was used as a positive control condition.

Single-cell RNA sequencing and TotalSeq sample preparation from KP tumors and healthy control lungs—KP tumors were induced in C57BL6/J mice by iv. injection of KP1.9 cells, and allowed to grow for 31 days before treating, or not, with aCD40. Two days after aCD40 treatment, the lungs of these mice were perfused, and tumor nodules were macroscopically dissected from the lungs and digested as described above to generate single cell suspensions. Healthy lungs were processed similarly. Cells were then stained with a combination of DNA-tagged TotalSeq-A antibodies and Hashtag antibodies (listed in the Key Resources Table), stained with a fluorochrome-labelled CD11b antibody for sorting,

and labelled with 7-AAD to identify live cells. $7AAD^{-}CD11b^{+}$ cells were sorted into PBS (no Ca or Mg) with 0.04% BSA, at a concentration of 1000–1500 cells/μL. After this, cells were processed with Chromium Next GEM Single Cell 3 'Kit v3.1, 4 rxns (PN-1000269) before loading on a Chromium Next GEM Chip G Single Cell Kit, 16 rxns (PN-1000127). In collaboration with the Single Cell Core Facility at Harvard Medical School, standard steps were followed for library preparation, quality control and amplification. Sequencing was performed in collaboration with the Biopolymers Facility at Harvard Medical School, using the NovaSeqSP platform (1,600,000,000 reads, 20k reads/cell).

Single-cell RNA sequencing sample preparation from MC38 tumors—MC38 tumors were harvested 2 days after aCD40 treatment. Tissues were digested as described above to generate single cell suspensions, cells were stained for CD45 and labeled with 7AAD (Sigma-Aldrich). $7AAD^{-}CD45^{+}$ cells were sorted using a BD FACSAria sorter. InDrops single cell RNA sequencing was performed as described previously[59,84,85]. Briefly, a microfluidic device was used to co-encapsulate individual cells and polyacrylamide beads carrying barcoding reverse transcription (RT) primers and lysis reagents into 2–3 nl droplets, followed by primer release and RT at 50°C. After the RT reaction, droplets were broken, and the resulting barcoded cDNA was taken through the following sequencing library preparation steps 1) second strand synthesis, 2) in vitro transcription providing linear amplification of the material, 3) fragmentation of the amplified RNA, 4) a second reverse transcription using random hexamer primers bearing a universal PCR primer annealing site, and 5) indexing PCR, yielding a sequencing-ready library. DNA sequences of primers used during the library preparation were described previously[59]. Libraries were sequenced on the NextSeq Illumina platform, paired-end mode, dual indexing.

Single-cell RNA-sequencing and TotalSeq analysis

scRNAseq read processing: For the KP tumor dataset, raw FASTQ files were processed by Cell Ranger 6.0.1 using mm10-2020 as a reference. Count matrices for transcripts, captured antibodies, and multiplexing tags were simultaneously generated using cellranger multi with default parameters. For the MC38 tumor dataset, the FASTQ files were processed using STARSolo[81].

Data filtering and normalization: For the KP tumor dataset, cells expressing >5% mitochondrial transcripts or fewer than 300 total transcripts were excluded as low-quality cells. Cells with transcript numbers above the 99th percentile within each experiment were considered potential doublets and excluded.

The MC38 tumor dataset was processed as described previously[59]. Specifically, library-specific thresholds on total counts (ranging from 120 to 400 counts) and fraction of counts coming from mitochondrial genes (ranging from 12% to 15%) were manually determined based on the empirical distributions of these magnitudes in each library.

For statistical analysis of both datasets, normalized counts per ten-thousand (*CP10K*) were used, except when indicated otherwise.

Dimensionality reduction and visualization: Separate embeddings were created for immune cells derived from healthy lungs and KP tumors combined, and from aCD40-treated KP tumors. Raw counts from healthy lung + KP tumor and aCD40-treated KP tumor were separately normalized through scTransform v1[78] after removing genes present in fewer than 3 cells per dataset. PCA (n=50) was applied on the Pearson residuals from scTransform. Neighbors-graphs (k=15) were constructed from the PC spaces of each dataset. 2D UMAP embeddings were generated from each KNN graph. The MC38 tumor dataset was processed following the pipeline detailed in Siwicki et al[59].

Identification of neutrophils: For the KP tumor dataset, a classifier was applied to the complete scRNAseq data set (including contaminating $CD11b^{+}$ non-neutrophil cells) to define the major immune cell type identity of each transcriptome. The classifier was trained on scRNAseq data from immune cells in KP lung tumors published earlier[24]. Correct annotation of major cell types and separation of neutrophils from non-neutrophil cell types was confirmed by inspection of the UMAP embedding and examination of cell type-specific marker gene expression. In addition, Total-Seq confirmed specific expression of Ly6G protein on cells classified as neutrophils, but not on cells annotated as non-neutrophils. In all analyses concerning neutrophil states, cells annotated as non-neutrophils were excluded. Cells from clusters with a majority of non-neutrophil cells were also excluded regardless of their initial annotation in order to prevent the inclusion of potential contaminants with ambiguous transcriptional identities. Cells from MC38 tumors were clustered using Scanpy's implementation of the Leiden algorithm and manually annotated into coarse immune subsets, including neutrophils, based on marker gene expression.

Identification of neutrophil states: A reference atlas of neutrophil states was constructed based on previously published scRNAseq data from KP tumors[24]. The neutrophil population "N1" originally identified in Zilionis et al.[24] represented a continuum of states whose variation proved important to resolve in order to correctly define changes after aCD40 immunotherapy in the current study. Specifically, Ngp^{hi} cells within the N1 state were enriched in many of the same genes as N6 cells and were directly connected to them in the nearest-neighbors graph. For this reason, the "N1" cluster was partitioned by sub-clustering into two clusters, which defined N1a ($Sell^{hi}Ngp^{hi}$) and N1b ($Sell^{hi}Lst1^{hi}$) neutrophils. The remaining neutrophil populations ("N2"-"N6") were left unchanged. Then, transcriptomes obtained in the current study from healthy lung, KP tumor, aCD40-treated KP tumor were classified through the method reported previously[24] using the constructed atlas as reference. Because N4 and N6 formed a continuum, we denoised the annotations by reclassifying as N4 any initially cell classified as N6 that neighbored at least one cell classified as N4. A single iteration of this denoising procedure was carried out, on each dataset separately (healthy lung + KP tumor, aCD40-treated KP tumor). Similarly, the state identity of neutrophils from MC38 tumors was inferred through classification.

Identification of marker genes for neutrophil states: For Figure 2B, Wilcoxon rank-sum test was used to identify differentially expressed genes in each neutrophil state in the aCD40-treated KP tumor condition. Genes with an FDR above 0.01 and a log fold change below 0.25 were excluded. The reference expression level ($CP10K_{ref}$) was calculated

for each gene, representing the second highest average expression among the neutrophil subpopulations in the aCD40-treated condition. Candidate marker genes were then ranked by their fold change

$$\left(log_2 \frac{CP10K + 1}{CP10K_{ref} + 1}\right)$$

relative to the second highest expression level. The top 100 marker genes for each neutrophil state identified by this method are shown in Fig. 2B, and all genes that passed the initial filter are listed in Table S1.

For Figures S3A and B, Wilcoxon rank-sum test was used to identify genes differentially expressed in each neutrophil state in the combined healthy lung + untreated KP tumor conditions. A series of filters was then applied to obtain the list of marker genes. Genes with fold-changes smaller than 2, expressed in fewer than 10% of the in-group cells, or expressed in over 50% of out-group cells were excluded. Remaining marker genes were then sorted by their normalized U statistic and the top 500 for each population were considered. Lastly, genes appearing in the top 500 of more than one sub-population were discarded. Top marker genes per neutrophil state identified using this method are shown in Figure S3A,B. The complete lists of marker genes for each neutrophil state in the healthy lung + untreated KP tumor dataset and in the aCD40-treated KP tumor dataset are shown in Table S1.

Quantifying the abundance of neutrophil states in untreated and aCD40-treated KP tumors: The number of neutrophils per mg of tissue corresponding to each neutrophil state (Fig. 3A) was estimated by multiplying the cross-replicate average fraction of each neutrophil state with the number of total neutrophils per milligram of tissue measured through flow cytometry.

Processing of antibody-derived tag data: Raw counts derived from the antibody panel were CLR (centered log ratio) transformed as described by Stoeckius et al.[39].

Interactive SPRING viewer: The data and embeddings associated with each condition are available for interactive exploration through SPRING[82]. Transcriptomic data is shown as normalized counts (CP10K), and surface marker expression is expressed as CLR-transformed counts. Links corresponding to each embedding are listed under Deposited Data in the Key Resources Table.

Quantifying the abundance of major immune subsets in untreated and treated MC38 tumors: For Fig. 1F and G, we quantified the abundance of each major immune cell type in untreated, aCD40-treated, and aPD-1-treated MC38 tumors as the fraction of all cells annotated as each cell type in each dataset. We report changes in abundance as the fold change between the abundances of each cell type in the treated and untreated condition for each referenced dataset. More explicitly, for each cell state i, the fold change FC(i) was computed as:

$$FC(i) = \frac{f^{(i)}_{treated}}{f^{(i)}_{untreated}} = \frac{n^{(i)}_{treated} / N_{treated}}{n^{(i)}_{untreated} / N_{untreated}}$$

Where f is the fraction of the cell type, n is the number of cells annotated to cell state i, and N is the total number of cells sampled.

Evaluating cell state similarities across studies: Cells annotated as neutrophils from each study were classified using an immune atlas as reference (see: Identification of neutrophil states), leading to all cells receiving a label from the reference. Cells classified as anything but a neutrophil subset or as states represented by fewer than 10 cells in a condition were not considered for further analysis. Using each condition as a reference at a time, the probability of classification of each cell with respect to each state from the reference was computed. Reciprocal similarity scores between each pair of states were computed as the harmonic mean of the average probabilities obtained by applying the classifier in both directions, as described previously[24,43].

Quantifying the abundance of Sell^{hi} neutrophils in untreated and treated tumors across tumor models: The abundance of *Sell*^{hi} neutrophils in each tumor model was determined by calculating the proportion of immune cells annotated as N1a, N1b, or N2 (see: Evaluating cell state similarities across studies) among the total number of immune cells present in each dataset. The change in the percentage of *Sell*^{hi} neutrophils between the treated and untreated conditions for each tumor model and treatment is depicted in Fig. 3D, where 0% represents no observed change. The untreated cells from each dataset were used as the reference for comparison.

Calculating gene set scores: Gene set scores were computed as the average expression of the genes belonging to each gene set of interest set minus the average expression of a control gene set, as described by Tirosh et al.[86] and implemented in Scanpy. For these calculations, log-normalized counts were standardized across all transcriptomes within each group of conditions (tumor-free + tumor-burdened, aCD40-treated). The resulting Z-scores were employed as the measure of relative expression of each gene. The gene sets underlying Fig. 4A–D are listed in Table S1.

The gene sets corresponding to angiogenesis, ECM remodeling, immunosuppression, tumor proliferation, and myeloid cell recruitment were obtained from Engblom et al. (2017)[9]. The genes corresponding to neutrophil cytotoxicity were selected from the gene ontology terms Neutrophil mediated cytotoxicity (GO:0070942) and Respiratory burst (GO:0045730). The genes correponding to neutrophil degranulation were selected from the gene ontology term Neutrophil degranulation (GO:0043312). The genes used to define the Interferon signaling scores were selected from the gene ontology terms Type I interferon-mediated signaling pathway (GO:0060337) and Interferon Gamma Response (MSigDB HallMark M5913). The genes used to define the neutrotime scores correspond to the early neutrotime genes from Grieshaber-Bouyer et al. (2021)[47] and are listed individually in Fig. 5D. For neutrotime scores, signs of the scores obtained from Scanpy were flipped so that higher scores would reflect a higher degree of maturity.

RNA velocity: Velocyto[49] was used under default parameters to generate splice-aware count matrices from the mapped reads from each library. Unspliced and spliced counts were matched to the barcodes retained after filtering and annotated as neutrophils in each library. Separate velocity embeddings were created for the healthy lung + KP tumor and the aCD40-treated KP tumor conditions. scVelo[48] was used to compute connectivities and velocities in each group of conditions. For the cells from the healthy lung + KP tumor dataset, all genes were employed in velocity calculations, and no subsequent filtering by R^2 was performed. For cells from aCD40-treated KP tumor, velocities were only computed for highly variable genes as determined by scVelo, and genes with a velocity R^2 smaller than 0.01 were excluded from graph calculations. The stochastic model was employed in both cases. Velocity graphs and visualizations were computed through scVelo based on pre-existing UMAP embeddings for each condition.

Transcription factor prediction: Prediction of active transcription factors was performed using the ChEA3 algorithm[87] based on enriched genes in N1a and N2 neutrophil states compared to all other neutrophil states in anti-CD40-treated KP tumors. Predicted transcription factors were ranked based on their average rank across all transcription factor-target gene libraries (mean rank).

Analysis of clinical data from STIMULI trial—We analyzed data from the 4–12 STIMULI clinical trial (NCT02046733) that was performed by the European Thoracic Oncology Platform (ETOP, https://www.etop-eu.org) in patients with limited-disease small-cell lung cancer. All patients received standard-of-care induction concomitant radio-chemotherapy (cis-/carboplatin + etoposide + thoracic radiotherapy) followed by consolidation therapy either with ipilimumab and nivolumab or by standard-of-care observation[61]. We focused on patients who received combination immunotherapy as consolidation (n=78). The neutrophil-to-lymphocyte ratio (NLR) was calculated as the ratio of the absolute counts (G/l) of neutrophils and lymphocytes in peripheral blood at enrolment (baseline NLR) and after radio-chemotherapy but before the first dose of immunotherapy (post-therapy NLR). NLR change was calculated as a percentage change comparing post-therapy NLR versus baseline NLR. From the 78 patients, 70 patients had available post-therapy NLR data for comparison with the baseline. Four patients showed disease progression following radio-chemotherapy and were excluded from the consolidation part as per protocol. Four patients had missing post-radio-chemotherapy NLR data. Kaplan-Meier estimates of survival were analyzed using the “survival” (version 3.3–1) and “survminer” (version 0.4.9) packages in RStudio. Hazard ratios of survival were calculated using univariate Cox regression in the “survival” R package.

Quantification and statistical analysis—Statistical analyses of data from mouse experiments were performed using GraphPad Prism, except for scRNAseq analyses for which details are provided in the respective methods sections. Analysis of clinical data was performed in RStudio. Statistical parameters (sample size, P-value, statistical test) for all analyses are reported in the corresponding figure legends.

Supplementary Material

Refer to Web version on PubMed Central for supplementary material.

Acknowledgments

We thank the Harvard Stem Cell Institute for help with FACS; the Single Cell Core Facility at Harvard Medical School for help with scRNAseq experiments; the Biopolymers Facility at Harvard Medical School for sequencing; the MGH Histopathology Research Core and Y. Iwamoto as well as the EPFL Histology Core Facility for processing, preparation and staining of mouse histological tissue specimens; G. J. Freeman for generously providing the anti-PD-1 antibody reagent; U. Von Andrian, R. Nowarski and S. Pai: and members of the Pittet and Weissleder laboratories for helpful discussions. We thank the patients who participated in the STIMULI trial, the staff at the ETOP Coordinating Office and the ETOP Statistical Office for providing the clinical data.

This work was supported in part by NIH grant R01-CA218579 (to A.M.K. and M.J.P.), NIH grant P01-CA240239 (to M.J.P.), and the ISREC Foundation (to M.J.P.). J.G. and M.S. were supported in part by Landry Cancer Biology Research Fellowships. R.B. was funded by a Postdoc.Mobility Fellowship and Return Grant of the Swiss National Science Foundation (SNSF; P400PM_183852; P5R5PM_203164). M.K. was supported by the EMBO Postdoctoral Fellowship (ALTF 662–2020) and the Human Frontier Science Program Postdoctoral Fellowship (LT000017/2021-L).

References

1. Ino Y, Yamazaki-Itoh R, Shimada K, Iwasaki M, Kosuge T, Kanai Y, and Hiraoka N (2013). Immune cell infiltration as an indicator of the immune microenvironment of pancreatic cancer. Brit J Cancer 108, 914–923. 10.1038/bjc.2013.32. [PubMed: 23385730]
2. Kargl J, Busch SE, Yang GHY, Kim K-H, Hanke ML, Metz HE, Hubbard JJ, Lee SM, Madtes DK, McIntosh MW, et al. (2017). Neutrophils dominate the immune cell composition in non-small cell lung cancer. Nature Communications 8, 1–11. 10.1038/ncomms14381.
3. Klemm F, Maas RR, Bowman RL, Kornete M, Soukup K, Nassiri S, Brouland J-P, Iacobuzio-Donahue CA, Brennan C, Tabar V, et al. (2020). Interrogation of the Microenvironmental Landscape in Brain Tumors Reveals Disease-Specific Alterations of Immune Cells. Cell 181, 1643–1660.e17. 10.1016/j.cell.2020.05.007. [PubMed: 32470396]
4. Schürch CM, Bhate SS, Barlow GL, Phillips DJ, Noti L, Zlobec I, Chu P, Black S, Demeter J, McIlwain DR, et al. (2020). Coordinated Cellular Neighborhoods Orchestrate Antitumoral Immunity at the Colorectal Cancer Invasive Front. Cell 183, 838. 10.1016/j.cell.2020.10.021. [PubMed: 33125896]
5. Shaul ME, and Fridlender ZG (2019). Tumour-associated neutrophils in patients with cancer. Nat Rev Clin Oncol 16, 601–620. 10.1038/s41571-019-0222-4. [PubMed: 31160735]
6. Siwicki M, and Pittet MJ (2021). Versatile neutrophil functions in cancer. Semin Immunol 57, 101538. 10.1016/j.smim.2021.101538. [PubMed: 34876331]
7. Albrengues J, Shields MA, Ng D, Park CG, Ambrico A, Poindexter ME, Upadhyay P, Uyeminami DL, Pommier A, Küttner V, et al. (2018). Neutrophil extracellular traps produced during inflammation awaken dormant cancer cells in mice. Science 361. 10.1126/science.aao4227.
8. Coffelt SB, Kersten K, Doornebal CW, Weiden J, Vrijland K, Hau C-S, Verstegen NJM, Ciampricotti M, Hawinkels LJAC, Jonkers J, et al. (2015). IL-17-producing γδ T cells and neutrophils conspire to promote breast cancer metastasis. Nature 522, 345–348. 10.1038/nature14282. [PubMed: 25822788]
9. Engblom C, Pfirschke C, Zilionis R, Martins JDS, Bos SA, Courties G, Rickelt S, Severe N, Baryawno N, Faget J, et al. (2017). Osteoblasts remotely supply lung tumors with cancer-promoting SiglecFhigh neutrophils. Science 358. 10.1126/science.aal5081.
10. Szczerba BM, Castro-Giner F, Vetter M, Krol I, Gkountela S, Landin J, Scheidmann MC, Donato C, Scherrer R, Singer J, et al. (2019). Neutrophils escort circulating tumour cells to enable cell cycle progression. Nature 566, 553–557. 10.1038/s41586-019-0915-y. [PubMed: 30728496]
11. Wellenstein MD, Coffelt SB, Duits DEM, Miltenburg M.H. van, Slagter M, Rink I. de, Henneman L, Kas SM, Prekovic S, Hau C-S, et al. (2019). Loss of p53 triggers Wnt-

dependent systemic inflammation to drive breast cancer metastasis. Nature 572, 538–542. 10.1038/s41586-019-1450-6. [PubMed: 31367040]

12. Yang L, Liu Q, Zhang X, Liu X, Zhou B, Chen J, Huang D, Li J, Li H, Chen F, et al. (2020). DNA of neutrophil extracellular traps promotes cancer metastasis via CCDC25. Nature 583, 133–138. 10.1038/s41586-020-2394-6. [PubMed: 32528174]
13. Cui C, Chakraborty K, Tang XA, Zhou G, Schoenfelt KQ, Becker KM, Hoffman A, Chang Y-F, Blank A, Reardon CA, et al. (2021). Neutrophil elastase selectively kills cancer cells and attenuates tumorigenesis. Cell 184, 3163–3177.e21. 10.1016/j.cell.2021.04.016. [PubMed: 33964209]
14. Fridlender ZG, Sun J, Kim S, Kapoor V, Cheng G, Ling L, Worthen GS, and Albelda SM (2009). Polarization of tumor-associated neutrophil phenotype by TGF-beta: “N1” versus “N2” TAN. Cancer Cell 16, 183–194. 10.1016/j.ccr.2009.06.017. [PubMed: 19732719]
15. Matlung HL, Babes L, Zhao XW, Houdt M. van, Treffers LW, Rees D.J. van, Franke K, Schornagel K, Verkuijlen P, Janssen H, et al. (2018). Neutrophils Kill Antibody-Opsonized Cancer Cells by Trogoptosis. Cell Reports 23, 3946–3959.e6. 10.1016/j.celrep.2018.05.082. [PubMed: 29949776]
16. Mysore V, Cullere X, Mears J, Rosetti F, Okubo K, Liew PX, Zhang F, Madera-Salcedo I, Rosenbauer F, Stone RM, et al. (2021). FcγR engagement reprograms neutrophils into antigen cross-presenting cells that elicit acquired anti-tumor immunity. Nat Commun 12, 4791. 10.1038/s41467-021-24591-x. [PubMed: 34373452]
17. Ponzetta A, Carriero R, Carnevale S, Barbagallo M, Molgora M, Perucchini C, Magrini E, Gianni F, Kunderfranco P, Polentarutti N, et al. (2019). Neutrophils Driving Unconventional T Cells Mediate Resistance against Murine Sarcomas and Selected Human Tumors. Cell 178, 346–360.e24. 10.1016/j.cell.2019.05.047. [PubMed: 31257026]
18. Singhal S, Bhojnagarwala PS, O’Brien S, Moon EK, Garfall AL, Rao AS, Quatromoni JG, Stephen TL, Litzky L, Deshpande C, et al. (2016). Origin and Role of a Subset of Tumor-Associated Neutrophils with Antigen-Presenting Cell Features in Early-Stage Human Lung Cancer. Cancer Cell 30, 120–135. 10.1016/j.ccell.2016.06.001. [PubMed: 27374224]
19. Quail DF, Amulic B, Aziz M, Barnes BJ, Eruslanov E, Fridlender ZG, Goodridge HS, Granot Z, Hidalgo A, Huttenlocher A, et al. (2022). Neutrophil phenotypes and functions in cancer: A consensus statement. J Exp Medicine 219, e20220011. 10.1084/jem.20220011.
20. Dinh HQ, Eggert T, Meyer MA, Zhu YP, Olingy CE, Llewellyn R, Wu R, and Hedrick CC (2020). Coexpression of CD71 and CD117 Identifies an Early Unipotent Neutrophil Progenitor Population in Human Bone Marrow. Immunity 53, 319–334.e6. 10.1016/j.immuni.2020.07.017. [PubMed: 32814027]
21. Mollaoglu G, Jones A, Wait SJ, Mukhopadhyay A, Jeong S, Arya R, Camolotto SA, Mosbruger TL, Stubben CJ, Conley CJ, et al. (2018). The Lineage-Defining Transcription Factors SOX2 and NKX2–1 Determine Lung Cancer Cell Fate and Shape the Tumor Immune Microenvironment. Immunity 49, 764–779.e9. 10.1016/j.immuni.2018.09.020. [PubMed: 30332632]
22. Shaul ME, Eyal O, Guglietta S, Aloni P, Zlotnik A, Forkosh E, Levy L, Weber LM, Levin Y, Pomerantz A, et al. (2020). Circulating neutrophil subsets in advanced lung cancer patients exhibit unique immune signature and relate to prognosis. Faseb J 34, 4204–4218. 10.1096/fj.201902467r. [PubMed: 31957112]
23. Zhu YP, Eggert T, Araujo DJ, Vijayanand P, Ottensmeier CH, and Hedrick CC (2020). CyTOF mass cytometry reveals phenotypically distinct human blood neutrophil populations differentially correlated with melanoma stage. J Immunother Cancer 8, e000473. 10.1136/jitc-2019-000473. [PubMed: 32912924]
24. Zilionis R, Engblom C, Pfirschke C, Savova V, Zemmour D, Saatcioglu HD, Krishnan I, Maroni G, Meyerovitz CV, Kerwin CM, et al. (2019). Single-Cell Transcriptomics of Human and Mouse Lung Cancers Reveals Conserved Myeloid Populations across Individuals and Species. Immunity 50, 1317–1334.e10. 10.1016/j.immuni.2019.03.009. [PubMed: 30979687]
25. Bassez A, Vos H, Dyck LV, Floris G, Arijs I, Desmedt C, Boeckx B, Bempt MV, Nevelsteen I, Lambein K, et al. (2021). A single-cell map of intratumoral changes during anti-PD1 treatment of patients with breast cancer. Nat Med 27, 820–832. 10.1038/s41591-021-01323-8. [PubMed: 33958794]

26. Bi K, He MX, Bakouny Z, Kanodia A, Napolitano S, Wu J, Grimaldi G, Braun DA, Cuoco MS, Mayorga A, et al. (2021). Tumor and immune reprogramming during immunotherapy in advanced renal cell carcinoma. Cancer Cell 39, 649–661.e5. 10.1016/j.ccell.2021.02.015. [PubMed: 33711272]
27. Duong E, Fessenden TB, Lutz E, Dinter T, Yim L, Blatt S, Bhutkar A, Wittrup KD, and Spranger S (2022). Type I interferon activates MHC class I-dressed CD11b+ conventional dendritic cells to promote protective anti-tumor CD8+ T cell immunity. Immunity 55, 308–323.e9. 10.1016/j.immuni.2021.10.020. [PubMed: 34800368]
28. Gubin MM, Esaulova E, Ward JP, Malkova ON, Runci D, Wong P, Noguchi T, Arthur CD, Meng W, Alspach E, et al. (2018). High-Dimensional Analysis Delineates Myeloid and Lymphoid Compartment Remodeling during Successful Immune-Checkpoint Cancer Therapy. Cell 175, 1014–1030.e19. 10.1016/j.cell.2018.09.030. [PubMed: 30343900]
29. Boivin G, Faget J, Ancey P-B, Gkasti A, Mussard J, Engblom C, Pfirschke C, Contat C, Pascual J, Vazquez J, et al. (2020). Durable and controlled depletion of neutrophils in mice. Nat Commun 11, 2762. 10.1038/s41467-020-16596-9. [PubMed: 32488020]
30. Kargl J, Zhu X, Zhang H, Yang GHY, Friesen TJ, Shipley M, Maeda DY, Zebala JA, McKay-Fleisch J, Meredith G, et al. (2019). Neutrophil content predicts lymphocyte depletion and anti-PD1 treatment failure in NSCLC. Jci Insight 4, e130850. 10.1172/jci.insight.130850. [PubMed: 31852845]
31. Kim IS, Gao Y, Welte T, Wang H, Liu J, Janghorban M, Sheng K, Niu Y, Goldstein A, Zhao N, et al. (2019). Immuno-subtyping of breast cancer reveals distinct myeloid cell profiles and immunotherapy resistance mechanisms. Nat Cell Biol 21, 1113–1126. 10.1038/s41556-019-0373-7. [PubMed: 31451770]
32. DuPage M, Dooley AL, and Jacks T (2009). Conditional mouse lung cancer models using adenoviral or lentiviral delivery of Cre recombinase. Nat Protoc 4, 1064–1072. 10.1038/nprot.2009.95. [PubMed: 19561589]
33. Horton BL, Morgan DM, Momin N, Zagorulya M, Torres-Mejia E, Bhandarkar V, Wittrup KD, Love JC, and Spranger S (2021). Lack of CD8+ T cell effector differentiation during priming mediates checkpoint blockade resistance in non–small cell lung cancer. Sci Immunol 6, eabi8800. 10.1126/sciimmunol.abi8800. [PubMed: 34714687]
34. Martinez-Usatorre A, Kadioglu E, Boivin G, Cianciaruso C, Guichard A, Torchia B, Zangger N, Nassiri S, Keklikoglou I, Schmittnaegel M, et al. (2021). Overcoming microenvironmental resistance to PD-1 blockade in genetically engineered lung cancer models. Sci Transl Med 13. 10.1126/scitranslmed.abd1616.
35. Pfirschke C, Engblom C, Rickelt S, Cortez-Retamozo V, Garris C, Pucci F, Yamazaki T, Poirier-Colame V, Newton A, Redouane Y, et al. (2016). Immunogenic Chemotherapy Sensitizes Tumors to Checkpoint Blockade Therapy. Immunity 44, 343–354. 10.1016/j.immuni.2015.11.024. [PubMed: 26872698]
36. Garris CS, Arlauckas SP, Kohler RH, Trefny MP, Garren S, Piot C, Engblom C, Pfirschke C, Siwicki M, Gungabeesoon J, et al. (2018). Successful Anti-PD-1 Cancer Immunotherapy Requires T Cell-Dendritic Cell Crosstalk Involving the Cytokines IFN-γ and IL-12. Immunity 49, 1148–1161.e7. 10.1016/j.immuni.2018.09.024. [PubMed: 30552023]
37. Moreno BH, Zaretsky JM, Garcia-Diaz A, Tsoi J, Parisi G, Robert L, Meeth K, Ndoye A, Bosenberg M, Weeraratna AT, et al. (2016). Response to Programmed Cell Death-1 Blockade in a Murine Melanoma Syngeneic Model Requires Costimulation, CD4, and CD8 T Cells. Cancer Immunol Res 4, 845–857. 10.1158/2326-6066.cir-16-0060. [PubMed: 27589875]
38. Jin Y, An X, Mao B, Sun R, Kumari R, Chen X, Shan Y, Zang M, Xu L, Muntel J, et al. (2022). Different syngeneic tumors show distinctive intrinsic tumor-immunity and mechanisms of actions (MOA) of anti-PD-1 treatment. Sci Rep-uk 12, 3278. 10.1038/s41598-022-07153-z.
39. Stoeckius M, Hafemeister C, Stephenson W, Houck-Loomis B, Chattopadhyay PK, Swerdlow H, Satija R, and Smibert P (2017). Simultaneous epitope and transcriptome measurement in single cells. Nat Methods 14, 865–868. 10.1038/nmeth.4380. [PubMed: 28759029]
40. Pfirschke C, Engblom C, Gungabeesoon J, Lin Y, Rickelt S, Zilionis R, Messemaker M, Siwicki M, Gerhard GM, Kohl A, et al. (2020). Tumor-Promoting Ly-6G+ SiglecFhigh Cells Are Mature

and Long-Lived Neutrophils. Cell Reports 32, 108164–108164. 10.1016/j.celrep.2020.108164. [PubMed: 32966785]

41. Gabaldón T (2008). Large-scale assignment of orthology: back to phylogenetics? Genome Biol 9, 235. 10.1186/gb-2008-9-10-235. [PubMed: 18983710]
42. Rivera MC, Jain R, Moore JE, and Lake JA (1998). Genomic evidence for two functionally distinct gene classes. Proc National Acad Sci 95, 6239–6244. 10.1073/pnas.95.11.6239.
43. Gerhard GM, Bill R, Messemaker M, Klein AM, and Pittet MJ (2020). Tumor-infiltrating dendritic cell states are conserved across solid human cancers. J Exp Medicine 218, e20200264. 10.1084/jem.20200264.
44. Groom JR, Richmond J, Murooka TT, Sorensen EW, Sung JH, Bankert K, von Andrian UH, Moon JJ, Mempel TR, and Luster AD (2012). CXCR3 Chemokine Receptor-Ligand Interactions in the Lymph Node Optimize CD4+ T Helper 1 Cell Differentiation. Immunity 37, 1091–1103. 10.1016/j.immuni.2012.08.016. [PubMed: 23123063]
45. Hidalgo A, Chilvers ER, Summers C, and Koenderman L (2019). The Neutrophil Life Cycle. Trends Immunol 40, 584–597. 10.1016/j.it.2019.04.013. [PubMed: 31153737]
46. Hidalgo A, and Casanova-Acebes M (2021). Dimensions of neutrophil life and fate. Semin Immunol 57, 101506. 10.1016/j.smim.2021.101506. [PubMed: 34711490]
47. Grieshaber-Bouyer R, Radtke FA, Cunin P, Stifano G, Levescot A, Vijaykumar B, Nelson-Maney N, Blaustein RB, Monach PA, Nigrovic PA, et al. (2021). The neutrotime transcriptional signature defines a single continuum of neutrophils across biological compartments. Nat Commun 12, 2856. 10.1038/s41467-021-22973-9. [PubMed: 34001893]
48. Bergen V, Lange M, Peidli S, Wolf FA, and Theis FJ (2020). Generalizing RNA velocity to transient cell states through dynamical modeling. Nat Biotechnol 38, 1408–1414. 10.1038/s41587-020-0591-3. [PubMed: 32747759]
49. Manno GL, Soldatov R, Zeisel A, Braun E, Hochgerner H, Petukhov V, Lidschreiber K, Kastriti ME, Lönnerberg P, Furlan A, et al. (2018). RNA velocity of single cells. Nature 560, 494–498. 10.1038/s41586-018-0414-6. [PubMed: 30089906]
50. Evrard M, Kwok IWH, Chong SZ, Teng KWW, Becht E, Chen J, Sieow JL, Penny HL, Ching GC, Devi S, et al. (2018). Developmental Analysis of Bone Marrow Neutrophils Reveals Populations Specialized in Expansion, Trafficking, and Effector Functions. Immunity 48, 364–379.e8. 10.1016/j.immuni.2018.02.002. [PubMed: 29466759]
51. Kwok I, Becht E, Xia Y, Ng M, Teh YC, Tan L, Evrard M, Li JLY, Tran HTN, Tan Y, et al. (2020). Combinatorial Single-Cell Analyses of Granulocyte-Monocyte Progenitor Heterogeneity Reveals an Early Uni-potent Neutrophil Progenitor. Immunity 53, 303–318.e5. 10.1016/j.immuni.2020.06.005. [PubMed: 32579887]
52. Manley HR, Keightley MC, and Lieschke GJ (2018). The Neutrophil Nucleus: An Important Influence on Neutrophil Migration and Function. Front Immunol 9, 2867. 10.3389/fimmu.2018.02867. [PubMed: 30564248]
53. Ioannou M, Hoving D, Aramburu IV, Temkin MI, Vasconcelos NMD, Tsourouktsoglou T-D, Wang Q, Boeing S, Goldstone R, Vernardis S, et al. (2022). Microbe capture by splenic macrophages triggers sepsis via T cell-death-dependent neutrophil lifespan shortening. Nat Commun 13, 4658. 10.1038/s41467-022-32320-1. [PubMed: 35945238]
54. Xie X, Shi Q, Wu P, Zhang X, Kambara H, Su J, Yu H, Park S-Y, Guo R, Ren Q, et al. (2020). Single-cell transcriptome profiling reveals neutrophil heterogeneity in homeostasis and infection. Nat Immunol 21, 1119–1133. 10.1038/s41590-020-0736-z. [PubMed: 32719519]
55. Forero A, Ozarkar S, Li H, Lee CH, Hemann EA, Nadjsombati MS, Hendricks MR, So L, Green R, Roy CN, et al. (2019). Differential Activation of the Transcription Factor IRF1 Underlies the Distinct Immune Responses Elicited by Type I and Type III Interferons. Immunity 51, 451–464.e6. 10.1016/j.immuni.2019.07.007. [PubMed: 31471108]
56. Broz ML, Binnewies M, Boldajipour B, Nelson AE, Pollack JL, Erle DJ, Barczak A, Rosenblum MD, Daud A, Barber DL, et al. (2014). Dissecting the Tumor Myeloid Compartment Reveals Rare Activating Antigen-Presenting Cells Critical for T Cell Immunity. Cancer Cell 26, 638–652. 10.1016/j.ccell.2014.09.007. [PubMed: 25446897]

57. Liu F, Wu HY, Wesselschmidt R, Kornaga T, and Link DC (1996). Impaired Production and Increased Apoptosis of Neutrophils in Granulocyte Colony-Stimulating Factor Receptor–Deficient Mice. Immunity 5, 491–501. 10.1016/s1074-7613(00)80504-x. [PubMed: 8934575]
58. Byrne KT, and Vonderheide RH (2016). CD40 Stimulation Obviates Innate Sensors and Drives T Cell Immunity in Cancer. Cell Reports 15, 2719–2732. 10.1016/j.celrep.2016.05.058. [PubMed: 27292635]
59. Siwicki M, Gort-Freitas NA, Messemaker M, Bill R, Gungabeesoon J, Engblom C, Zilionis R, Garris C, Gerhard GM, Kohl A, et al. (2021). Resident Kupffer cells and neutrophils drive liver toxicity in cancer immunotherapy. Sci Immunol 6. 10.1126/sciimmunol.abi7083.
60. Chow MT, Ozga AJ, Servis RL, Frederick DT, Lo JA, Fisher DE, Freeman GJ, Boland GM, and Luster AD (2019). Intratumoral Activity of the CXCR3 Chemokine System Is Required for the Efficacy of Anti-PD-1 Therapy. Immunity 50, 1498–1512.e5. 10.1016/j.immuni.2019.04.010. [PubMed: 31097342]
61. Peters S, Pujol J-L, Dafni U, Dómine M, Popat S, Reck M, Andrade J, Becker A, Moro-Sibilot D, Curioni-Fontecedro A, et al. (2022). Consolidation nivolumab and ipilimumab versus observation in limited-disease small-cell lung cancer after chemo-radiotherapy – results from the randomised phase II ETOP/IFCT 4–12 STIMULI trial. Ann Oncol 33, 67–79. 10.1016/j.annonc.2021.09.011. [PubMed: 34562610]
62. Templeton AJ, McNamara MG, Šeruga B, Vera-Badillo FE, Aneja P, Ocaña A, Leibowitz-Amit R, Sonpavde G, Knox JJ, Tran B, et al. (2014). Prognostic Role of Neutrophil-to-Lymphocyte Ratio in Solid Tumors: A Systematic Review and Meta-Analysis. Jnci J National Cancer Inst 106, dju124. 10.1093/jnci/dju124.
63. Capone M, Giannarelli D, Mallardo D, Madonna G, Festino L, Grimaldi AM, Vanella V, Simeone E, Paone M, Palmieri G, et al. (2018). Baseline neutrophil-to-lymphocyte ratio (NLR) and derived NLR could predict overall survival in patients with advanced melanoma treated with nivolumab. J Immunother Cancer 6, 74. 10.1186/s40425-018-0383-1. [PubMed: 30012216]
64. Ghislat G, Cheema AS, Baudoin E, Verthuy C, Ballester PJ, Crozat K, Attaf N, Dong C, Milpied P, Malissen B, et al. (2021). NF-κB–dependent IRF1 activation programs cDC1 dendritic cells to drive antitumor immunity. Sci Immunol 6. 10.1126/sciimmunol.abg3570.
65. Kalafati L, Kourtzelis I, Schulte-Schrepping J, Li X, Hatzioannou A, Grinenko T, Hagag E, Sinha A, Has C, Dietz S, et al. (2020). Innate Immune Training of Granulopoiesis Promotes Anti-tumor Activity. Cell 183, 771–785.e12. 10.1016/j.cell.2020.09.058. [PubMed: 33125892]
66. Pilato MD, Kfuri-Rubens R, Pruessmann JN, Ozga AJ, Messemaker M, Cadilha BL, Sivakumar R, Cianciaruso C, Warner RD, Marangoni F, et al. (2021). CXCR6 positions cytotoxic T cells to receive critical survival signals in the tumor microenvironment. Cell 184, 4512–4530.e22. 10.1016/j.cell.2021.07.015. [PubMed: 34343496]
67. Lebratti T, Lim YS, Cofie A, Andhey P, Jiang X, Scott J, Fabbrizi MR, Ozantürk AN, Pham C, Clemens R, et al. (2021). A sustained type I IFN-neutrophil-IL-18 axis drives pathology during mucosal viral infection. Elife 10, e65762. 10.7554/elife.65762. [PubMed: 34047696]
68. Rocha BC, Marques PE, Leoratti F.M. de S., Junqueira C, Pereira DB, Antonelli L.R. do V., Menezes GB, Golenbock DT, and Gazzinelli RT (2015). Type I Interferon Transcriptional Signature in Neutrophils and Low-Density Granulocytes Are Associated with Tissue Damage in Malaria. Cell Reports 13, 2829–2841. 10.1016/j.celrep.2015.11.055. [PubMed: 26711347]
69. Vafadarnejad E, Rizzo G, Krampert L, Arampatzi P, Arias-Loza A-P, Nazzal Y, Rizakou A, Knochenhauer T, Bandi SR, Nugroho VA, et al. (2020). Dynamics of Cardiac Neutrophil Diversity in Murine Myocardial Infarction. Circ Res 127, e232–e249. 10.1161/circresaha.120.317200. [PubMed: 32811295]
70. Granot Z, Gershkovitz M, Caspi Y, Fainsod-Levi T, Katz B, Michaeli J, Khawaled S, Lev S, Polyansky L, Shaul ME, et al. (2018). TRPM2 mediates neutrophil killing of disseminated tumor cells. Cancer Res 78, canres.3614.2017. 10.1158/0008-5472.can-17-3614.
71. Granot Z, Henke E, Comen EA, King TA, Norton L, and Benezra R (2011). Tumor Entrained Neutrophils Inhibit Seeding in the Premetastatic Lung. Cancer Cell 20, 300–314. 10.1016/j.ccr.2011.08.012. [PubMed: 21907922]

72. Sionov RV, Fainsod-Levi T, Zelter T, Polyansky L, Pham CT, and Granot Z (2019). Neutrophil Cathepsin G and Tumor Cell RAGE Facilitate Neutrophil Anti-Tumor Cytotoxicity. Oncoimmunology 8, e1624129. 10.1080/2162402x.2019.1624129. [PubMed: 31428521]
73. Eruslanov EB, Bhojnagarwala PS, Quatromoni JG, Stephen TL, Ranganathan A, Deshpande C, Akimova T, Vachani A, Litzky L, Hancock WW, et al. (2014). Tumor-associated neutrophils stimulate T cell responses in early-stage human lung cancer. J Clin Invest 124, 5466–5480. 10.1172/jci77053. [PubMed: 25384214]
74. Blaisdell A, Crequer A, Columbus D, Daikoku T, Mittal K, Dey SK, and Erlebacher A (2015). Neutrophils Oppose Uterine Epithelial Carcinogenesis via Debridement of Hypoxic Tumor Cells. Cancer Cell 28, 785–799. 10.1016/j.ccell.2015.11.005. [PubMed: 26678340]
75. Shaul ME, Levy L, Sun J, Mishalian I, Singhal S, Kapoor V, Horng W, Fridlender G, Albelda SM, and Fridlender ZG (2016). Tumor-associated neutrophils display a distinct N1 profile following TGFβ modulation: A transcriptomics analysis of pro- vs. antitumor TANs. Oncoimmunology 5, e1232221. 10.1080/2162402x.2016.1232221. [PubMed: 27999744]
76. Hancock WW, Lu B, Gao W, Csizmadia V, Faia K, King JA, Smiley ST, Ling M, Gerard NP, and Gerard C (2000). Requirement of the Chemokine Receptor CXCR3 for Acute Allograft Rejection. J Exp Medicine 192, 1515–1520. 10.1084/jem.192.10.1515.
77. Wolf FA, Angerer P, and Theis FJ (2018). SCANPY: large-scale single-cell gene expression data analysis. Genome Biol 19, 15. 10.1186/s13059-017-1382-0. [PubMed: 29409532]
78. Hafemeister C, and Satija R (2019). Normalization and variance stabilization of single-cell RNA-seq data using regularized negative binomial regression. Genome Biol 20, 296. 10.1186/s13059-019-1874-1. [PubMed: 31870423]
79. Waskom M (2021). seaborn: statistical data visualization. J Open Source Softw 6, 3021. 10.21105/joss.03021.
80. Stuart T, Butler A, Hoffman P, Hafemeister C, Papalexi E, Mauck WM, Hao Y, Stoeckius M, Smibert P, and Satija R (2019). Comprehensive Integration of Single-Cell Data. Cell 177, 1888–1902.e21. 10.1016/j.cell.2019.05.031. [PubMed: 31178118]
81. Dobin A, Davis CA, Schlesinger F, Drenkow J, Zaleski C, Jha S, Batut P, Chaisson M, and Gingeras TR (2013). STAR: ultrafast universal RNA-seq aligner. Bioinformatics 29, 15–21. 10.1093/bioinformatics/bts635. [PubMed: 23104886]
82. Weinreb C, Wolock S, and Klein AM (2018). SPRING: a kinetic interface for visualizing high dimensional single-cell expression data. Bioinformatics 34, 1246–1248. 10.1093/bioinformatics/btx792. [PubMed: 29228172]
83. Bankhead P, Loughrey MB, Fernández JA, Dombrowski Y, McArt DG, Dunne PD, McQuaid S, Gray RT, Murray LJ, Coleman HG, et al. (2017). QuPath: Open source software for digital pathology image analysis. Sci Rep-uk 7, 16878. 10.1038/s41598-017-17204-5.
84. Zilionis R, Nainys J, Veres A, Savova V, Zemmour D, Klein AM, and Mazutis L (2017). Single-cell barcoding and sequencing using droplet microfluidics. Nat Protoc 12, 44–73. 10.1038/nprot.2016.154. [PubMed: 27929523]
85. Klein AM, Mazutis L, Akartuna I, Tallapragada N, Veres A, Li V, Peshkin L, Weitz DA, and Kirschner MW (2015). Droplet Barcoding for Single-Cell Transcriptomics Applied to Embryonic Stem Cells. Cell 161, 1187–1201. 10.1016/j.cell.2015.04.044. [PubMed: 26000487]
86. Tirosh I, Venteicher AS, Hebert C, Escalante LE, Patel AP, Yizhak K, Fisher JM, Rodman C, Mount C, Filbin MG, et al. (2016). Single-cell RNA-seq supports a developmental hierarchy in human oligodendroglioma. Nature 539, 309–313. 10.1038/nature20123. [PubMed: 27806376]
87. Keenan AB, Torre D, Lachmann A, Leong AK, Wojciechowicz ML, Utti V, Jagodnik KM, Kropiwnicki E, Wang Z, and Ma'ayan A (2019). ChEA3: transcription factor enrichment analysis by orthogonal omics integration. Nucleic Acids Res 47, W212–W224. 10.1093/nar/gkz446. [PubMed: 31114921]

Highlights:

- Neutrophils can acutely accumulate in tumors during successful immunotherapy
- Therapy expands a distinct neutrophil state with an IFN-stimulated gene signature
- The neutrophil response requires IRF1 and supports tumor control
- Therapy-elicited neutrophil response in patients is associated with better outcome

Successful cancer immunotherapy is associated with high numbers of neutrophils and expression of IRF-1.

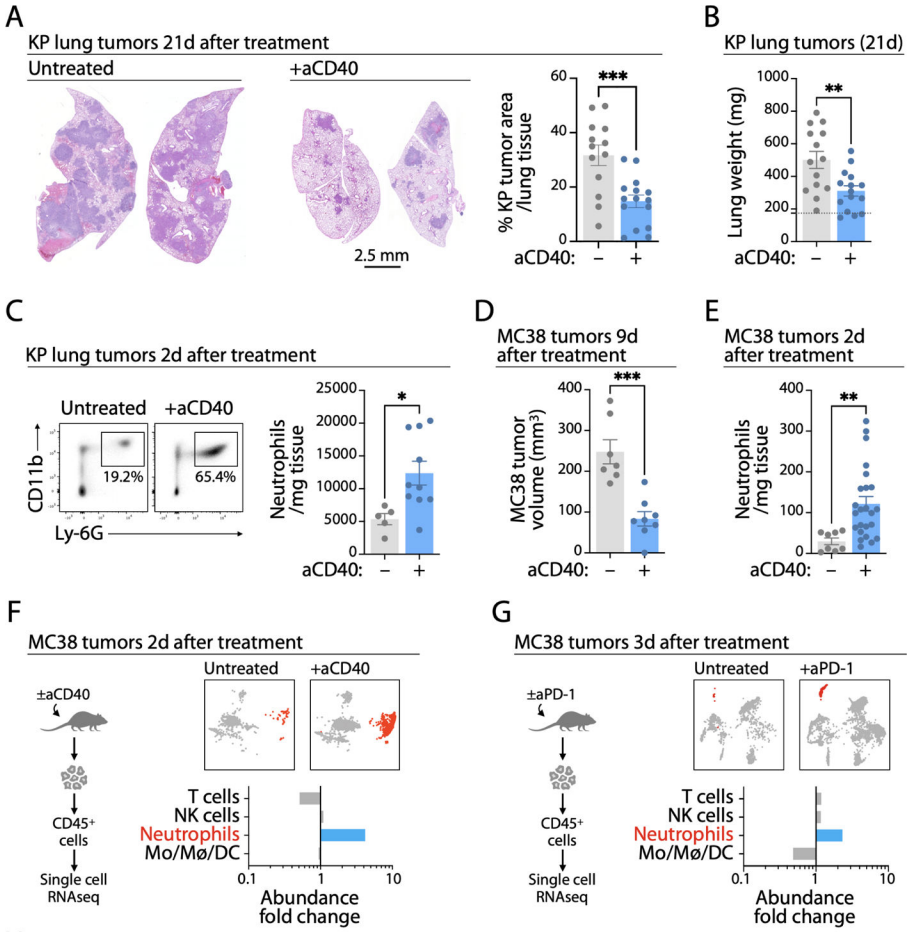

H

Summary of data

Tumor	Treatment	Tumor control		Neutrophil accumulation	
KP	aPD-1/CTLA-4	No	−4 ± 53%	No	−29 ± 9%
KP	aCD40	Yes	−53 ± 7%	Yes	+131 ± 34%
KP	Pac./Carbo.	No	+1 ± 7%	No	+14 ± 8%
KP	Oxa./Cyc.	Yes	−73 ± 10%	Yes	+140 ± 12%
MC38	aPD-1	Yes	−61 ± 5%	Yes	+173 ± 65%
MC38	aCD40	Yes	−66 ± 7%	Yes	+310 ± 60%

Figure 1. Neutrophils accumulate in tumors in the context of successful therapy.

(A) Representative images of hematoxylin and eosin-stained lung sections and quantification of KP lung tumor burden, 21 days after aCD40 treatment (n=13 untreated, n=15 aCD40-treated, data pooled from two independent experiments).

(B) Lung weight (proxy of tumor burden) of KP tumor-bearing mice, treated or not with aCD40 (n=14 untreated, n=15 aCD40-treated, data pooled from two independent experiments). Dashed line indicates average lung weight in tumor-free mice.

(C) Flow cytometry-based quantification of neutrophils in KP tumors, 2 days after aCD40 treatment (n=5 untreated, n=10 aCD40-treated; data pooled from three independent experiments). Representative dot plots of live $CD45^+$ cells are shown.

(D) Tumor volume of aCD40-treated and untreated MC38 tumor-bearing mice, 9 days after treatment (n=7 untreated, n=8 aCD40-treated).

(E) Flow cytometry-based quantification of neutrophils in MC38 tumors, 2 days after aCD40 treatment (n=8 untreated, n=24 aCD40-treated, data pooled from four independent experiments).

(F) scRNAseq-based profiling of $CD45^+$ cells in MC38 tumors, 2 days after aCD40 treatment (n=2 per group). Abundance of major immune cell subsets is quantified as fold change between aCD40-treated versus untreated conditions. Neutrophils are indicated in red in the UMAP.

(G) scRNAseq-based profiling of $CD45^+$ cells in MC38 tumors, 3 days after aPD-1 treatment (n=2 per group). Abundance of major immune cell subsets is quantified as fold change between aPD-1-treated versus untreated conditions. Neutrophils are indicated in red in the UMAP.

(H) Summary of assessed tumor models and treatments, showing quantification of tumor control and neutrophil accumulation. Pac./Carbo.: Paclitaxel/Carboplatin. Oxa./Cyc.: Oxaliplatin/Cyclophosphamide. Table shows mean ±SEM.

Bar graphs show mean ±SEM. For comparisons between two groups, Student's two tailed t-test was used. *P < 0.05; **P < 0.01; ***P < 0.001

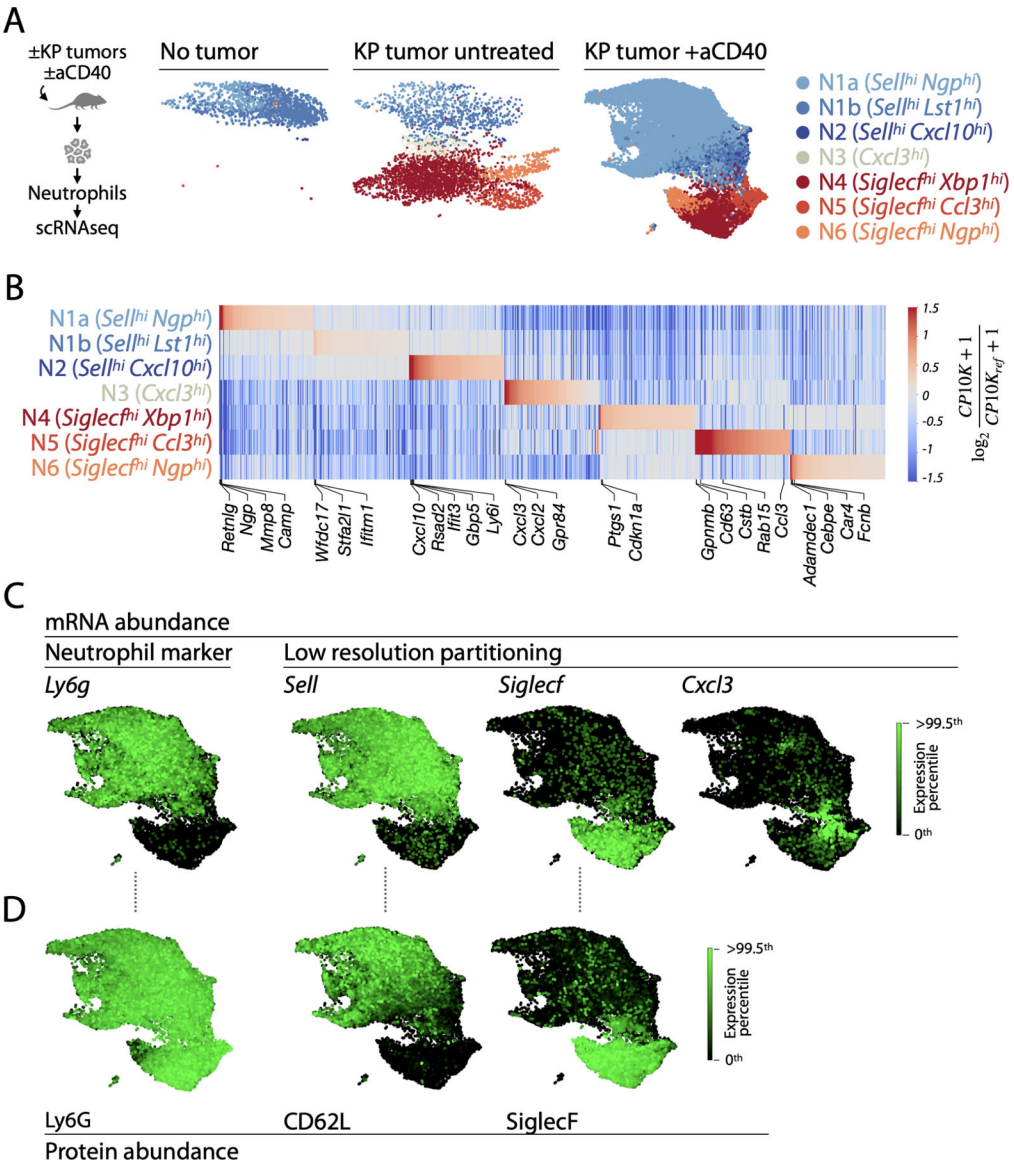

Figure 2. States of immunotherapy-elicited neutrophils in KP tumors

(A) scRNA-seq workflow, and uniform manifold approximation and projection (UMAP) visualization of neutrophil single-cell transcriptomes in lungs of healthy mice (n=2), KP tumor-bearing mice (n=2), and aCD40-treated KP tumor-bearing mice (n=2). A full list of marker genes for each neutrophil state is shown in Table S1.

(B) Enriched genes within neutrophil states in aCD40-treated KP tumor-bearing lungs shown in Figure 2A. Data underlying heatmap is shown in Table S1.

(C) mRNA expression of *Ly6g* and key markers used for low resolution partitioning of neutrophil states into three higher-level clusters.

(D) Protein expression of corresponding surface proteins encoded by the marker genes shown in panel C.

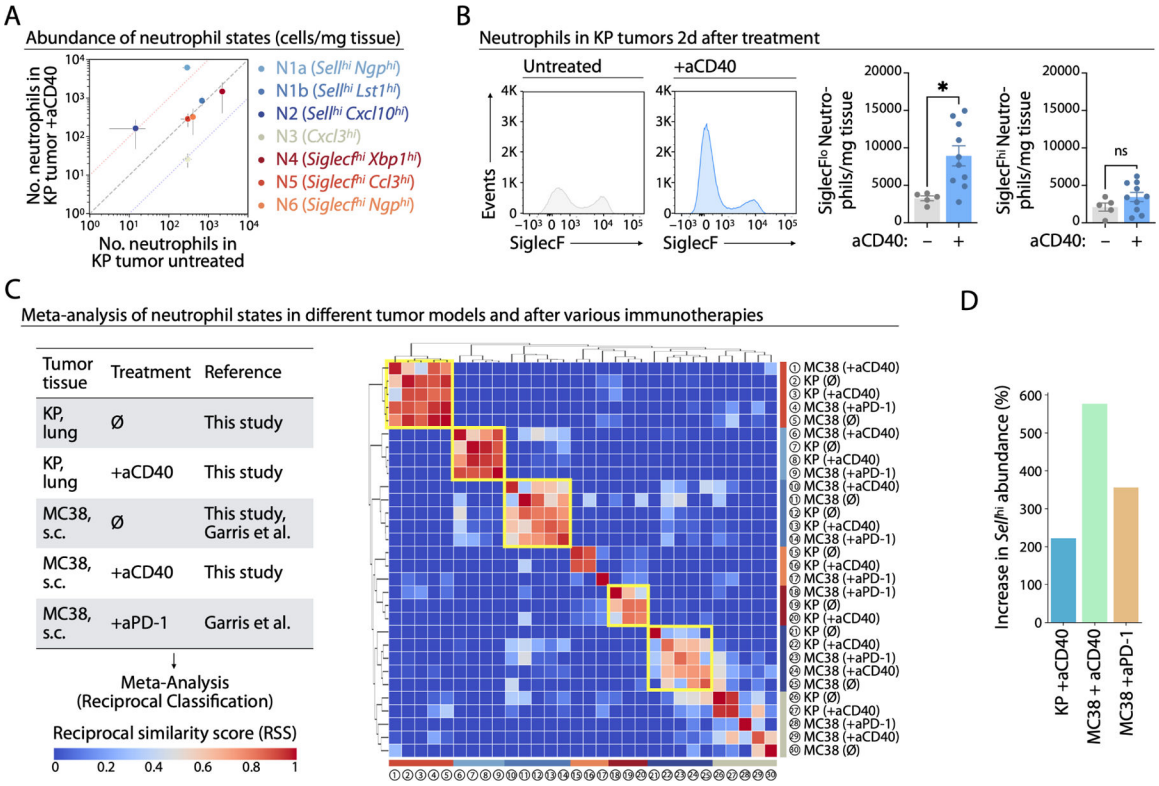

Figure 3. A subset of *Sell*^{hi} neutrophils expands in the context of successful immunotherapy

(A) Frequency of neutrophil states in KP tumors from aCD40-treated mice versus untreated mice, quantified as cells/mg tissue (n=2 per group). Dotted lines indicate 10-fold enrichment/depletion.

(B) Representative flow cytometry histogram of SiglecF expression by neutrophils in KP tumors 2 days after aCD40 treatment. Quantification of SiglecF^{lo} and SiglecF^{hi} neutrophils in KP tumors of untreated or aCD40-treated mice (n=5 untreated, n=10 aCD40-treated, data pooled from three independent experiments). Graphs show mean ±SEM. For comparisons between groups, Student's two tailed t-test was used. *P < 0.05.

(C) Heatmap showing reciprocal similarity scores calculated by cross-comparing tumor neutrophil states from the scRNAseq datasets listed in the table. Orthologous states are highlighted in yellow.

(D) Quantification of changes in abundance of orthologous *Sell*^{hi} neutrophil states in KP and MC38 tumors after aCD40 or aPD-1 treatment based on scRNAseq data shown in panel C.

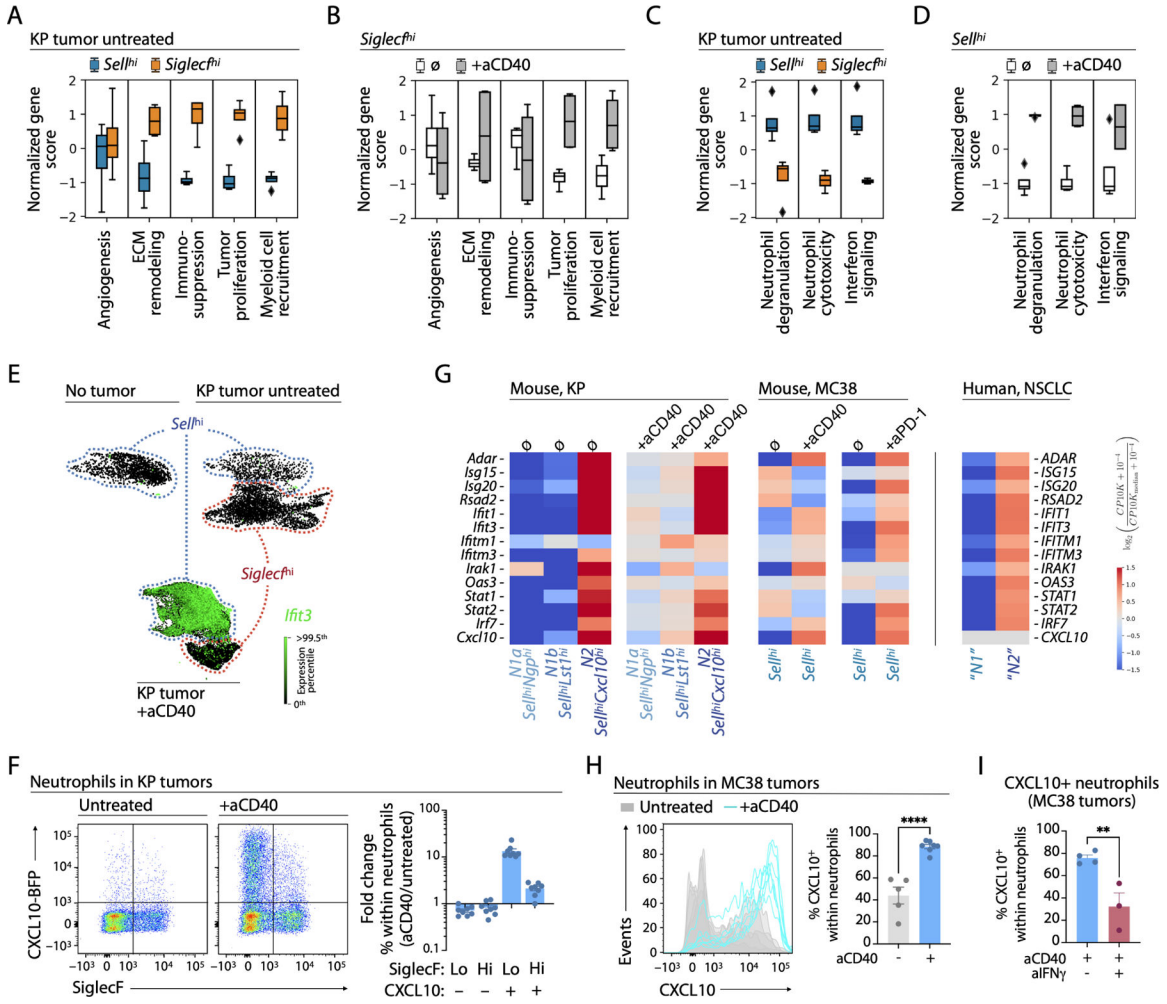

Figure 4. Neutrophils elicited by immunotherapy acquire an interferon-stimulated gene signature

(A) Expression of pro-tumor gene sets in *Sell*^{hi} and *Siglecf*^{hi} neutrophil states in untreated KP tumors.

(B) Expression of pro-tumor gene sets in *Siglecf*^{hi} neutrophils in untreated and aCD40-treated KP tumors.

(C) Expression of anti-tumor gene sets in *Sell*^{hi} and *Siglecf*^{hi} neutrophil states in untreated KP tumors.

(D) Expression of anti-tumor gene sets in *Siglecf*^{hi} neutrophils in untreated and aCD40-treated KP tumors.

(E) mRNA expression of the ISG *Ifit3* in neutrophils in healthy, untreated tumor-bearing, and aCD40-treated tumor-bearing lungs. *Sell*^{hi} states are circled in blue. *Siglecf*^{hi} states are circled in red.

(F) Representative flow cytometry dot plots showing CXCL10-BFP and SiglecF expression by neutrophils in KP tumors, before and after aCD40 treatment in REX3 transgenic mice. Fold changes in relative abundance (% within neutrophils) of neutrophil subsets defined by CXCL10 and SiglecF in response to treatment are plotted (n=4 untreated, n=8 aCD40-treated; data are pooled from two independent experiments).

(G) Heatmaps showing expression of ISGs by orthologous *Sell*^{hi} neutrophil states in KP tumors (untreated or aCD40-treated), and MC38 tumors (untreated, aCD40-treated, or aPD1-treated). In human NSCLC, the N1 neutrophil state is orthologous to mouse *Sell*^{hi} *Ngp*^{hi} and *Sell*^{hi} *Lst1*^{hi} neutrophils, and the N2 state is orthologous to *Sell*^{hi} *Cxcl10*^{hi} neutrophils.

(H) Flow cytometry histogram and quantification showing the change in CXCL10-BFP expression by neutrophils in MC38 tumors before and after aCD40 treatment in REX3 transgenic mice (n=5 untreated, n=7 aCD40-treated, data are pooled from two independent experiments).

(I) Proportion of CXCL10-BFP^{+} neutrophils in MC38 tumors with or without administration of neutralizing anti-IFNγ antibody during aCD40 treatment (n=4 untreated, n=3 aCD40-treated, data pooled from two independent experiments).

Box and whiskers plots in panel A-D show 95% CI. Bar graphs in panel F, H, I show mean ±SEM. For comparisons between two groups, Student's two tailed t-test was used. **P < 0.01; ****P < 0.0001

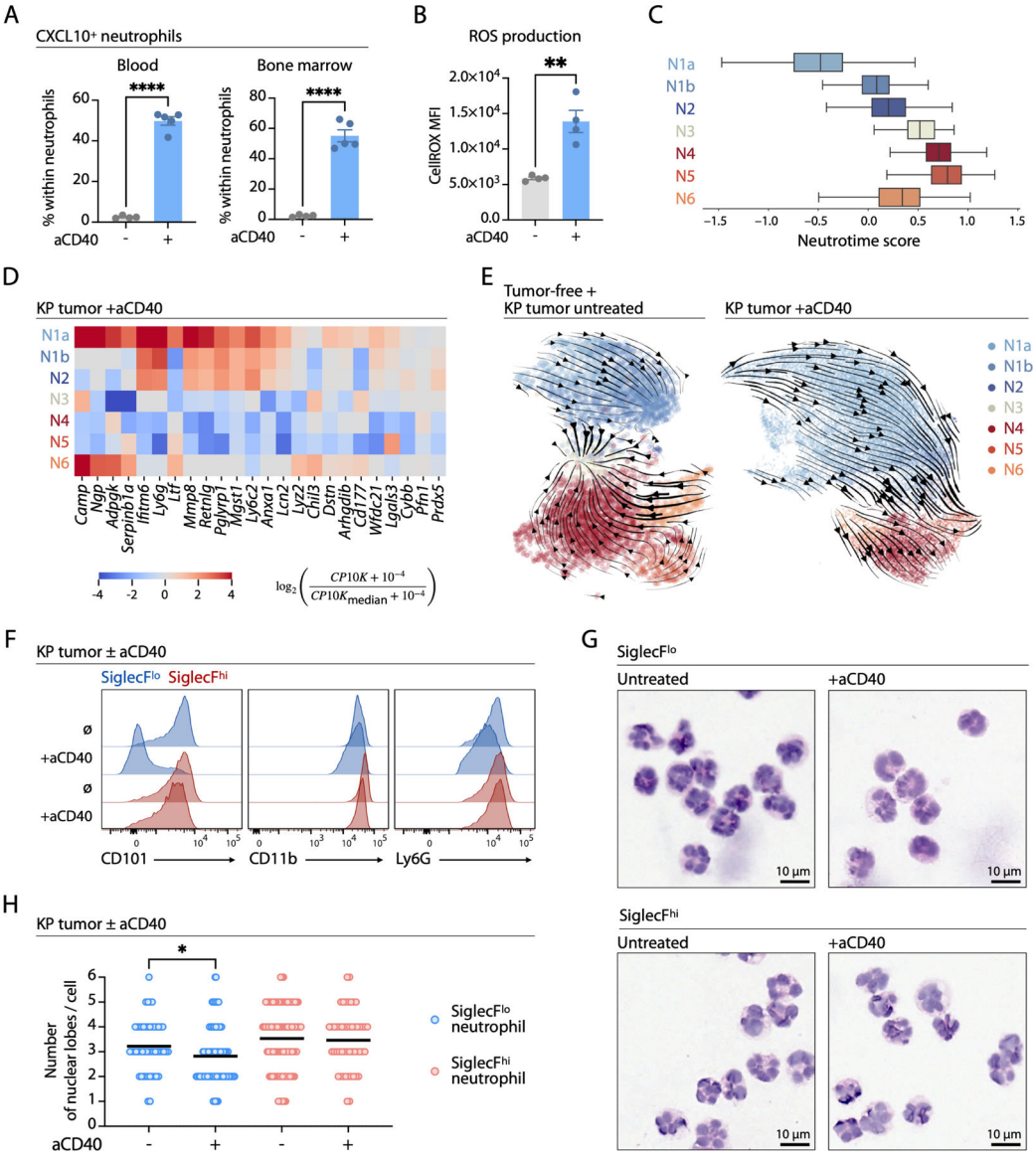

Figure 5. Immunotherapy-elicited neutrophils show a distinct phenotype and maturation state

(A) Proportion of CXCL10-BFP^{+} neutrophils in the blood and bone marrow of KP tumor-bearing mice with or without aCD40 treatment (n=4 untreated, n=5 aCD40-treated).

(B) ROS production in blood neutrophils of KP tumor-bearing mice with or without aCD40 treatment measured via CellROX fluorescence assay using flow cytometry (n=4 per group). MFI: median fluorescence intensity.

(C) Neutrotime score, indicating maturity, for each neutrophil state in aCD40-treated KP tumors. Box and whiskers plot shows 95% CI.

(D) Heatmap shows expression of individual early neutrotime genes across neutrophil states in aCD40-treated KP tumors.

(E) RNA velocity trajectories for neutrophil states in KP tumors of untreated or aCD40-treated mice.

(F) Representative histograms of CD101, CD11b and Ly6G expression on distinct neutrophil subsets in KP tumors with or without aCD40 treatment, assessed by flow cytometry.

(G) Representative images of hematoxylin and eosin-stained sorted neutrophils following cytospin.

(H) Quantification of nuclear lobes in different neutrophil subsets (n=50–100 cells per condition).

Graphs show mean ±SEM in panels A,B, graph shows mean in panel H. Panel A, B: Student's two tailed t-test. Panel H: Mann-Whitney test. *P<0.05; **P < 0.01; ****P < 0.0001

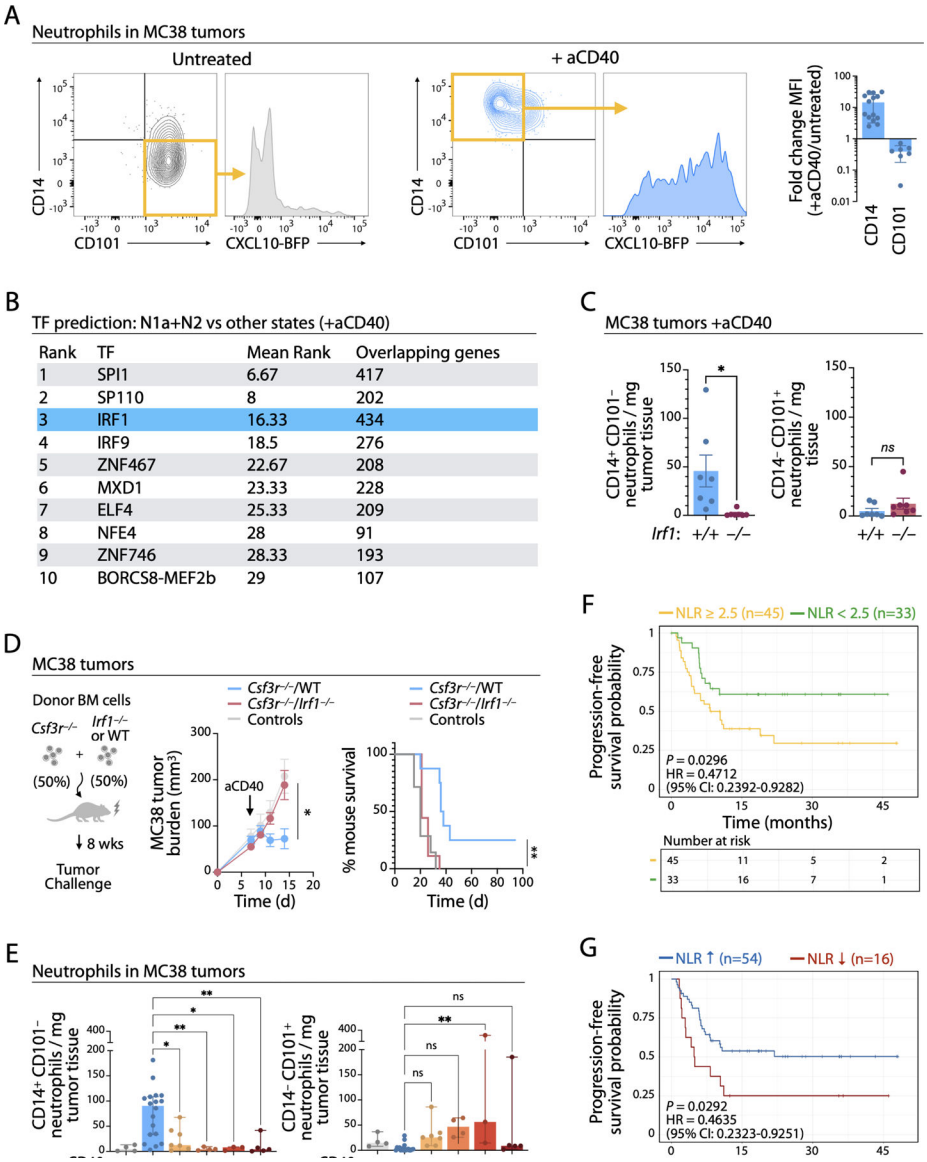

Rank	TF	Mean Rank	Overlapping genes
1	SPI1	6.67	417
2	SP110	8	202
3	IRF1	16.33	434
4	IRF9	18.5	276
5	ZNF467	22.67	208
6	MXD1	23.33	228
7	ELF4	25.33	209
8	NFE4	28	91
9	ZNF746	28.33	193
10	BORCS8-MEF2b	29	107

Figure 6. A neutrophil IRF1-mediated interferon response is required for tumor control in mice and a systemic therapy-induced neutrophil response correlates with good outcome in patients

(A) Left: Representative flow cytometry plots showing CD14, CD101 and CXCL10 expression in neutrophils in MC38 tumors with or without aCD40 treatment. Right: Quantification showing the change in expression of CD14 and CD101 on neutrophils in MC38 tumors upon aCD40 treatment (n=8–12 untreated, n=7–14 aCD40-treated, data pooled from three independent experiments). Graph shows mean ± SEM. MFI: median fluorescence intensity.

(B) Transcription factors predicted to be active in aCD40-expanded neutrophil states (N1a and N2) compared to all other states in KP tumors.

(C) Flow cytometry-based quantification of $CD14^{+}$ $CD101^{-}$ and $CD14^{-}$ $CD101^{+}$ neutrophils in MC38 tumors induced by aCD40 treatment, in the presence or absence of *Irf1* (n=7 per group, data pooled from two independent experiments). Graph shows mean ± SEM. Student's two-tailed t-test. *P < 0.05

(D) Schematic outlining the generation of bone marrow chimeras with *Irf1*-deficiency specifically in neutrophils. MC38 tumor volumes and survival of *Csf3r*$^{-/-}$/WT (control), aCD40-treated *Csf3r*$^{-/-}$/WT, and aCD40-treated *Csf3r*$^{-/-}$/*Irf1*$^{-/-}$ bone marrow chimeras (n=7–9 mice/group). Ordinary one-way ANOVA was used for tumor growth curve, and Log-rank (Mantel-Cox) test was used for the survival curve. *P < 0.05; **P < 0.01;
(E) Effect of *Batf3* deletion, *Il12b* deletion, IFNγ neutralization or *Cxcr3* deletion on the abundance of CD14^{+} CD101^{-} and CD14^{-} CD101^{+} neutrophils in MC38 tumors treated with aCD40 (n=3–18 per group, data pooled from six independent experiments). Graph shows median and 95% confidence interval. For comparisons between conditions, ordinary one-way ANOVA with Dunnett's multiple comparisons test was used. *P < 0.05; **P < 0.01.
(F) Kaplan-Meier plot of progression-free survival of small-cell lung cancer patients treated with chemo-radiotherapy and ipilimumab+nivolumab immunotherapy (n=78), separated by baseline neutrophil to lymphocyte ratio (NLR).
(G) Kaplan-Meier plot of progression-free survival of small-cell lung cancer patients treated with chemo-radiotherapy and ipilimumab+nivolumab immunotherapy (n=70), separated by NLR change post-chemo-radiotherapy versus baseline (NLR increase / NLR decrease: min. 10% change vs. baseline). Panels F and G: univariate Cox regression.

KEY RESOURCES TABLE

REAGENT or RESOURCE	SOURCE	IDENTIFIER
Antibodies		
Anti-mouse CD40 (Clone FGK4.5)	BioXCell	BE0016-2; RRID: AB_1107601
Anti-Mouse PD-1 (clone 29F.1A12)	Gordon J. Freeman	N/A
Anti-mouse CTLA-4 (clone 9D9)	BioXCell	BE0164; RRID: AB_10949609
Anti-mouse IFNγ (clone XMG1.2)	BioXCell	BE0055; RRID: AB_1107694
Anti-mouse Ly6G (clone 1A8)	BioXCell	BP0075; RRID: AB_10312146
Anti-mouse CD45 (clone 30-F11)	Biolegend	103126; RRID: AB_493535
Anti-mouse Ly6G (clone 1A8)	Biolegend	127643; RRID: AB_2565971
Anti-mouse CD11b (clone M1/70)	BD Biosciences	557657; RRID: AB_396772
Anti-mouse SiglecF (clone E50-2440)	BD Biosciences	564514; RRID: AB_2738833
Anti-mouse CD14 (clone Sa14-2)	Biolegend	123312; RRID: AB_940575
Anti-mouse CD101 (clone Moushi101)	eBioscience	25–1011-82; RRID: AB_2573378
Anti-mouse CXCR4 (clone L276F12)	Biolegend	146509; RRID: AB_2562786
Anti-mouse Ly6C (clone HK1.4)	Biolegend	128014; RRID: AB_1732079
Anti-mouse F4/80 (clone BM8)	Biolegend	Cat# 123114, RRID:AB_893478
Anti-mouse CD11c (clone N418)	Biolegend	Cat# 117334, RRID:AB_2562415
Anti-mouse I-A/I-E (clone M5/114.15.2)	Biolegend	Cat# 107608, RRID:AB_313323
Anti-mouse CD172a (clone P84)	Biolegend	Cat#144021, RRID:AB_2650812
Anti-mouse CD62L (clone MEL-14)	Biolegend	Cat#104411, RRID:AB_313098
Anti-mouse CD3ε (clone 145–2C11)	Biolegend	Cat#100308, RRID:AB_312673
Anti-mouse CD19 (clone 1D3/CD19)	Biolegend	Cat#152407, RRID: AB_2629816
Anti-mouse NK1.1 (clone PK136)	Biolegend	Cat#108707, RRID: AB_313394
Anti-mouse CXCR2 (clone SA044G4)	Biolegend	Cat#149313, RRID: AB_2734210
Anti-mouse CD4 (clone RM4-5)	BD Biosciences	Cat# 553051, RRID:AB_398528
Anti-mouse CD8a (clone 53–6.7)	BioLegend	Cat# 100730, RRID:AB_493703
Purified rat anti-mouse Ly-6G Antibody	Biolegend	127602; RRID: AB_1089180
Purified goat anti-mouse MPO Antibody	Biotechne/R&D systems	AF3667
Purified anti-mouse CD8a Antibody	eBioscience	14–0808-82; RRID: AB_2572861
TotalSeq™-A0013 anti-mouse Ly-6C Ab (clone HK1.4)	Biolegend	128047; RRID: AB_2749961
TotalSeq™-A0431 anti-mouse CD170 (Siglec-F) Ab (clone S17007L)	Biolegend	155513; RRID: AB_2832540
TotalSeq™-A0424 anti-mouse CD14 Ab (clone Sa14-2)	Biolegend	123333; RRID: AB_2800591
TotalSeq™-A0444 anti-mouse CD184 (CXCR4) Ab (clone L276F12)	Biolegend	146520; RRID: AB_2800682
TotalSeq™-A anti-mouse CXCR2 Ab (clone SA044G4)	Biolegend	N/A
TotalSeq™-A0105 anti-mouse CD115 (CSF-1R) Ab (clone AFS98)	Biolegend	135533; RRID: AB_2734198
TotalSeq™-A0190 anti-mouse CD274 (B7-H1, PD-L1) Ab (clone MIH6)	Biolegend	153604; RRID: AB_2783125
TotalSeq™-A0117 anti-mouse I-A/I-E Ab (clone M5/114.15.2)	Biolegend	107653; RRID: AB_2750505

REAGENT or RESOURCE	SOURCE	IDENTIFIER
TotalSeq™-A0104 anti-mouse CD102 (ICAM-2) Ab (clone 3C4 (MIC2/4))	Biolegend	105613; RRID: AB_2734167
TotalSeq™-A0074 anti-mouse CD54 (ICAM-1) Ab (clone YN1/1.7.4)	Biolegend	116127; RRID: AB_2734177
TotalSeq™-A0557 anti-mouse CD38 Ab (clone 90)	Biolegend	102733; RRID: AB_2750556
TotalSeq™-A0595 anti-mouse CD11a Ab (clone M17/4)	Biolegend	101125; RRID: AB_2783036
TotalSeq™-A0112 anti-mouse CD62L Ab (clone MEL-14)	Biolegend	104451; RRID: AB_2750364
TotalSeq™-A0201 anti-mouse CD103 Ab (clone 2E7)	Biolegend	121437; RRID: AB_2750349
TotalSeq™-A0200 anti-mouse CD86 Ab (clone GL-1)	Biolegend	105047; RRID: AB_2750348
TotalSeq™-A0114 anti-mouse F4/80 Ab (clone BM8)	Biolegend	123153; RRID: AB_2749986
TotalSeq™-A0078 anti-mouse CD49d Ab (clone R1–2)	Biolegend	103623; RRID: AB_2734159
TotalSeq™-A0012 anti-mouse CD117 (c-kit) Ab (clone 2B8)	Biolegend	105843; RRID: AB_2749960
TotalSeq™-A0015 anti-mouse Ly-6G Ab (clone 1A8)	Biolegend	127655; RRID: AB_2749962
TotalSeq™-A0093 anti-mouse CD19 Ab (clone 6D5)	Biolegend	115559; RRID: AB_2749981
TotalSeq™-A0238 Rat IgG2a, κ Isotype Ctrl Ab (clone RTK2758)	Biolegend	400571; RRID: N/A
TotalSeq™-A0301 anti-mouse Hashtag 1 Ab (clone M1/42)	Biolegend	155801; RRID: AB_2750032
TotalSeq™-A0302 anti-mouse Hashtag 2 Ab (clone M1/42)	Biolegend	155803; RRID: AB_2750033
TotalSeq™-A0303 anti-mouse Hashtag 3 Ab (clone M1/42)	Biolegend	155805; RRID: AB_2750034
TruStain fcX Anti-Mouse CD16/32 (clone 93)	Biolegend	101319; RRID: AB_1574973
Rabbit Anti-Rat IgG Antibody, Biotinylated	Vector Laboratories	BA-4001; RRID: N/A
Anti-Ly-6G MicroBeads UltraPure, mouse	Miltenyi Biotec	130–120-337; RRID: N/A
Donkey anti-goat Alexa 647	ThermoFisher Scientific	A21447
Goat anti-rat Alexa568	ThermoFisher Scientific	A11077
Chemicals, peptides, and recombinant proteins		
Standard LPS, E. coli 0111:B4	Invivogen	tlrl-eblps
Poly(I:C) HMW	Invivogen	tlrl-pic
Recombinant Murine IFN-γ	PeProtech	315–05
Recombinant Mouse IFN-β1 (carrier-free)	Biolegend	581302
7-Aminoactinomycin D	Sigma	A9400-1MG
ACK lysis buffer	Lonza	10–548E
Zombie Aqua™ Fixable Viability Kit	Biolegend	423102
Zombie Green™ Fixable Viability Kit	Biolegend	423111
Paclitaxel	McKesson	769014
Carboplatin	McKesson	724932
Oxaliplatin	McKesson	1090455
Cyclophosphamide	Sigma-Aldrich	C0768–1G
Retrievagen A (pH6.0)	BD Biosciences	550524
VECTASTAIN® Elite® ABC-HRP Kit, Peroxidase	Vector Laboratories	PK-6100
AEC+ Substrate-Chromogen	Agilent	K3469

REAGENT or RESOURCE	SOURCE	IDENTIFIER
Hematoxylin Solution, Harris Modified	Sigma	HHS32
Strepravidin DyLight 594	Vector Laboratories SA-5594	
DAPI	ThermoFisher Scientific	D21490
Immpress HRP Ready-to-use	Vector Laboratories	MP-7444-15
FluoromountG	Bioconcept	0100–01
Recombinant Mouse Flt3L	Peprotech	550704
TLR7/8 agonist R848	Invivogen	tlrl-r848
CellROX Green Flow Cytometry Assay Kit	Invitrogen	C10492
Critical commercial assays		
Chromium Next GEM Chip G Single Cell Kit, 16 rxns	10x Genomics	Cat# 1000127
Chromium Next GEM Single Cell 3′ Kit v3.1, 4 rxns	10x Genomics	Cat# 1000269
QuadroMACS™ Separator and Starting Kits	Miltenyi Biotec	Cat# 130–091-051
Deposited data		
Raw Single Cell RNA Sequencing Data - CD11b$^+$ cells from mouse KP lung tumors +/− aCD40 immunotherapy and healthy lungs	This paper	GEO: GSE224399
Raw Single Cell RNA Sequencing Data - CD45$^+$ cells from mouse MC38 tumors +/− aCD40 immunotherapy	This paper	GEO: GSE224400
Raw Single Cell RNA Sequencing Data - CD45$^+$ cells from mouse MC38 tumors +/− aPD1 immunotherapy	Garris et al.[36]	GEO: GSE112865
Single Cell RNA Sequencing Data (raw counts) - CD45$^+$ cells from human lung tumors	Zilionis et al.[24]	GEO: GSE127465
Interactive browser of CD11b$^+$ cells from lungs of healthy mice (gene expression - CP10K)	This paper	https://kleintools.hms.harvard.edu/tools/springViewer_1_6_dev.html?datasets/SPRING_private/gungabeesoon22/all_cells_healthy_gex/gex
Interactive browser of CD11b$^+$ cells from lungs of healthy mice (surface protein expression - CLR)	This paper	https://kleintools.hms.harvard.edu/tools/springViewer_1_6_dev.html?datasets/SPRING_private/gungabeesoon22/all_cells_healthy_adt/adt
Interactive browser of CD11b$^+$ cells from lungs of KP1.9 tumor-bearing mice (gene expression - CP10K)	This paper	https://kleintools.hms.harvard.edu/tools/springViewer_1_6_dev.html?datasets/SPRING_private/gungabeesoon22/all_cells_kp19_gex/gex
Interactive browser of CD11b$^+$ cells from lungs of KP1.9 tumor-bearing mice (surface protein expression - CLR)	This paper	https://kleintools.hms.harvard.edu/tools/springViewer_1_6_dev.html?datasets/SPRING_private/gungabeesoon22/all_cells_kp19_adt/adt
Interactive browser of CD11b$^+$ cells from lungs of KP1.9 tumor-bearing mice after aCD40 immunotherapy (gene expression - CP10K)	This paper	https://kleintools.hms.harvard.edu/tools/springViewer_1_6_dev.html?datasets/SPRING_private/gungabeesoon22/all_cells_acd40_gex/gex
Interactive browser of CD11b$^+$ cells from lungs of KP1.9 tumor-bearing mice after aCD40 immunotherapy (surface protein expression - CLR)	This paper	https://kleintools.hms.harvard.edu/tools/springViewer_1_6_dev.html?datasets/SPRING_private/gungabeesoon22/all_cells_acd40_adt/adt
Interactive browser of neutrophils from lungs of healthy mice (gene expression - CP10K)	This paper	https://kleintools.hms.harvard.edu/tools/springViewer_1_6_dev.html?datasets/SPRING_private/gungabeesoon22/neutrophils_healthy_gex/gex

REAGENT or RESOURCE	SOURCE	IDENTIFIER
Interactive browser of neutrophils from lungs of healthy mice (surface protein expression - CLR)	This paper	https://kleintools.hms.harvard.edu/tools/springViewer_1_6_dev.html?datasets/SPRING_private/gungabeesoon22/neutrophils_healthy_adt/adt
Interactive browser of neutrophils from lungs of KP1.9 tumor-bearing mice (gene expression - CP10K)	This paper	https://kleintools.hms.harvard.edu/tools/springViewer_1_6_dev.html?datasets/SPRING_private/gungabeesoon22/neutrophils_kp19_gex/gex
Interactive browser of neutrophils from lungs of KP1.9 tumor-bearing mice (surface protein expression - CLR)	This paper	https://kleintools.hms.harvard.edu/tools/springViewer_1_6_dev.html?datasets/SPRING_private/gungabeesoon22/neutrophils_kp19_adt/adt
Interactive browser of neutrophils from lungs of KP1.9 tumor-bearing mice after aCD40 immunotherapy (gene expression - CP10K)	This paper	https://kleintools.hms.harvard.edu/tools/springViewer_1_6_dev.html?datasets/SPRING_private/gungabeesoon22/neutrophils_acd40_gex/gex
Interactive browser of neutrophils from lungs of KP1.9 tumor-bearing mice after aCD40 immunotherapy (surface protein expression - CLR)	This paper	https://kleintools.hms.harvard.edu/tools/springViewer_1_6_dev.html?datasets/SPRING_private/gungabeesoon22/neutrophils_acd40_adt/adt
Interactive browser of $CD45^+$ cells from MC38 tumors either untreated or treated with aCD40 immunotherapy (gene expression - CP10K)	This paper	https://kleintools.hms.harvard.edu/tools/springViewer_1_6_dev.html?datasets/SPRING_private/gungabeesoon22/all_cells_mc38_pm_acd40/gex
Interactive browser of neutrophils from MC38 tumors either untreated or treated with aCD40 immunotherapy (gene expression - CP10K)	This paper	https://kleintools.hms.harvard.edu/tools/springViewer_1_6_dev.html?datasets/SPRING_private/gungabeesoon22/neutrophils_mc38_pm_acd40/gex
Experimental models: Cell lines		
Murine MC38 colorectal carcinoma cell line	Mark J. Smyth	RRID: CVCL_B288
Murine MC38-H2B-GFP	Ralph Weissleder	N/A
Murine KP1.9 lung adenocarcinoma cell line derived from lung tumor nodules of a C57BL/6$Kras^{LSL\text{-}G12D/WT}$;$p53^{Flox/Flox}$ mouse	Alfred Zippelius	N/A
Experimental models: Organisms/strains		
Mouse: WT C57BL/6J	The Jackson Laboratory	Strain# 000664 RRID:IMSR_JAX:000664
Mouse: B6.129S(C)-*Batf3*^{tm1Kmm}/J	The Jackson Laboratory	Strain #:013755 RRID:IMSR_JAX:013755
Mouse: B6.129S1-*Il12b*^{tm1Jm}/J	The Jackson Laboratory	Strain #:002693 RRID:IMSR_JAX:002693
Mouse: B6.129-Il12b^{tm1Lky}/J	The Jackson Laboratory	Strain# 006412 RRID:IMSR_JAX:006412
Mouse: B6.129X1(Cg)-*Csf3r*^{tm1Link}/J	The Jackson Laboratory	Strain #:017838 RRID:IMSR_JAX:017838
Mouse: B6.129S2-*Irf1*^{tm1Mak}/J	The Jackson Laboratory	Strain #:002762 RRID:IMSR_JAX:002762
Mouse: REX3 Transgenic	Andrew D. Luster	Groom et al. (2012)[44]
Mouse: $Kras^{LSL\text{-}G12D/+}$;$Trp53^{flox/flox}$	Tyler Jacks	DuPage et al. (2009)[32]
Mouse: B6.129S4-Ifng$^{tm3.1Lky}$/J	The Jackson Laboratory	Strain#017581 RRID:IMSR_JAX:017581
Mouse: Cxcr3^{tm1Wwh}	Andrew D. Luster	Hancock et al. (2000)[76]

REAGENT or RESOURCE	SOURCE	IDENTIFIER
Software and algorithms		
Python 3.8.13	Python Software foundation	https://www.python.org
R 4.1.1	R Core	https://www.r-project.org/
Scanpy 1.8.2	Wolf et al. (2018)[77]	https://github.com/scverse/scanpy
sctransform 0.3.2	Hafemeister and Satija (2019)[78]	https://github.com/satijalab/sctransform
Seaborn 0.11.2	Waskom (2021)[79]	https://seaborn.pydata.org/
Seurat 4.0.6	Stuart et al. (2019)[80]	https://github.com/satijalab/seurat/releases/tag/v4.0.6
STARsolo 2.7	Dobin et al. (2013)[81]	https://github.com/alexdobin/STAR/blob/master/docs/STARsolo.md
SPRING	Weinreb et al.v(2018)[82]	https://github.com/AllonKleinLab/SPRING_dev
FlowJo v.10.8	FlowJo, LLC	RRID: SCR_008520
Graphpad Prism v.9	GraphPad Prism	RRID: SCR_002798
FIJI ImageJ Version 2.1.0/1.53c	FIJI	RRID: SCR_002285
QuPath v0.4.0 Digital Pathology	Bankhead et al. (2017)[83]	RRID:SCR_018257
Code used for scRNAseq analyses	This study	https://github.com/AllonKleinLab/ifn_neutrophils/tree/main/notebooks